Binding Energies of Hydrated Cobalt(II) By Collision-Induced Dissociation and

Theoretical Studies: Evidence for a New Critical Size

Rebecca A. Coates and P. B. Armentrout*

Department of Chemistry, University of Utah, 315 S. 1400 E. Rm 2020, Salt Lake City, UT 84112

ABSTRACT

The experimental sequential bond energies for loss of water from $Co^{2+}(H_2O)_x$ complexes,

x = 5 - 11, are determined by threshold collision-induced dissociation (TCID) using a guided ion

beam tandem mass spectrometer with a thermal electrospray ionization source. Kinetic energy

dependent TCID cross sections are analyzed to yield 0 K thresholds for sequential loss of neutral

water molecules. The thresholds are converted from 0 to 298 K values to give hydration enthalpies

and free energies. Theoretical geometry optimizations and single point energy calculations at

several levels of theory are performed for the reactant and product ion complexes. Theoretical

bond energies for ground structures are used for direct comparison with experimental values to

obtain structural information on these complexes. In addition, the dissociative charge separation

process, $Co^{2+}(H_2O)_x \rightarrow CoOH^+(H_2O)_m + H^+(H_2O)_{x-m-1}$, is observed at x = 4, 6, and 7 in competition

with primary water loss products. Energies for the charge separation rate-limiting transition states

are calculated and compared to experimental threshold measurements. Results suggest that the

critical size for which charge separation is energetically favored over water loss is $x_{crit} = 6$, in

contrast to lower values in previous literature reports.

INTRODUCTION

Transition metals play important roles in many chemical and biological systems. Although metals can be essential for life, they can also become toxic in high concentrations from excessive intake. Humans mainly obtain transition metals from the environment through breathing air, drinking water, and eating food that contains such metals. As such, metal ion interactions with these media have become the subject of extensive research in order to understand the fundamentals of these intermolecular interactions. For the past several years, the Armentrout group has studied the thermochemistry of the hydration of many transition metal dications, $M^{2+}(H_2O)_x$ where M = Fe, 1 Ni, 2 Cu, 3 Zn, 4 , 5 and Cd, 6 , 7 and MOH⁺(H₂O)_x where $M = Co^8$ and Cu⁹ in the gas-phase using threshold collision-induced dissociation (TCID) complemented by theoretical calculations. Such thermochemistry has also been explored by several other research groups using different techniques including blackbody infrared radiative dissociation, 10 , 11 collision-induced dissociation, $^{12-14}$ and ion equilibria. $^{15-17}$

The present study extends our TCID studies to complete the late 3d transition metal dication hydration energies by examining the sequential dissociation of $Co^{2+}(H_2O)_x$ complexes, where x = 5 - 11. Understanding the hydration of Co^{2+} is vital as cobalt is an essential element for life, e.g., the core of vitamin B12,¹⁸ yet can be toxic if consumed in excess of 1 mg/kg.¹⁹ In agreement with our previous $M^{2+}(H_2O)_x$ studies, the dominant process observed upon activation of the cobalt complexes studied is reaction 1, loss of a single water ligand,

$$M^{2+}(H_2O)_x \to M^{2+}(H_2O)_{x-1} + H_2O$$
 (1)

followed by sequential loss of additional water molecules. In addition, $M^{2+}(H_2O)_x$ complexes of particular sizes that depend on the metal identity are found to undergo dissociative charge separation processes, reactions 2.

$$M^{2+}(H_2O)_x \to MOH^+(H_2O)_m + H^+(H_2O)_{x-m-1}$$
 (2)

Some interest in reaction 2 has focused on determining the minimum size at which water loss is favored over charge separation. This critical size, x_{crit} , has been defined as "the maximum number of ligands at which dissociative charge transfer is competitive with simple ligand loss." For hydrated cobalt dications, Kebarle and coworkers reported that the largest complex size for which dissociative charge separation occurred was a lower limit of 4, 12, 16, 17 whereas Shvartzburg and Siu suggested $x_{crit} = 5$. He may more precisely defining the critical size as "the largest value of x at which the charge separation is energetically favored over the loss of one water ligand", previous studies in our laboratory have determined the energy-dependent x_{crit} for late 3d transition metals: 4 for Fe²⁺, 4 for Ni²⁺, 8 for Cu²⁺, and 7 for Zn²⁺. As will be shown below, the present study determines x_{crit} for Co²⁺(H₂O)_x using the energy-dependent definition as $x_{crit} = 6$. This value of x_{crit} is consistent with the findings of O'Brien and Williams, in which laser-induced photodissociation at 215 K of Co²⁺(H₂O)_x for x = 5 - 8 resulted in 90%, 70%, 0% and 0%, respectively, of the photodissociation products formed via charge separation. In

As detailed below, TCID experiments with complementary theoretical calculations are used in the present work to establish hydration energies and the threshold energies for charge separation, which allows identification of the critical size and coordination number (CN) of hydrated Co²⁺. In contrast to our previous hydrated 3d transition metal dication studies, ¹⁻⁷ the present work shows evidence for Co²⁺(H₂O)_x complexes in which H₂O molecules start to occupy the second shell even though the first shell is not completely closed. Such detailed understanding of the hydration structure, aqueous reactivity, and periodic trends of transition metals can provide insight into the roles and transport of these metals in biological systems and environmental remediation.

EXPERIMENTAL AND COMPUTATIONAL METHODS

Experimental Procedures. Cross sections for the CID of hydrated cobalt dication complexes are measured using a guided ion beam tandem mass spectrometer (GIBMS), which has been described in detail previously.^{20, 21} The hydrated cobalt dications, $Co^{2+}(H_2O)_x$, are created

from a 10⁻⁴ M solution of CoCl₂ in pure water using an electrospray ionization (ESI) source.²² The solution is pumped through a stainless steel needle at a low flow rate of 0.08 - 0.10 L/h and an applied voltage of 2.0 - 2.2 kV. Ions then enter the vacuum system through an inlet cap and drift through a capillary heated to 80 °C to promote desolvation of large droplets. The ions that emerge from the capillary are collected and focused into an 88 plate radiofrequency (rf) ion funnel (IF),²³ with a DC gradient typically 8 - 12 V. Ions are injected from the IF into an rf-only hexapole ion guide (6P) that traps the ions in the radial direction with an rf amplitude of 250 V peak-to-peak. An in-source fragmentation technique utilizing negatively biased dc electrodes in between the hexapole rods, as described in detail elsewehere,²⁴ was used to effectively enhance the signal intensity of smaller M²⁺(H₂O)_r complexes by fragmenting larger complexes. However, increasing the voltage beyond the peak intensity for the x = 5 complex resulted primarily in dissociation to form charge separation products rather than water loss. This phenomenon was also seen previously for $Ni^{2+}(H_2O)_x$, $^2Cu^{2+}(H_2O)_x$, and $Zn^{2+}(H_2O)_x$ complexes. It has been postulated this is partly a result of the relatively high second ionization energies (IEs) for these late 3d transition metals, 17.1 – 20.3 eV.²⁵ As a result, we were unable to create $Co^{2+}(H_2O)_x$ complexes where $x \le 4$ with appreciable intensity for further study. Once past the electrodes, the ions undergo >10⁴ collisions with ambient gas as they drift through the hexapole ion guide. Previous studies have shown that under the proper conditions, the ions emerging from the hexapole are thermalized to room temperature. ^{2, 6, 24, 26-30} To further investigate the thermalization of the ions, a 5.1 cm long nitrogen gas cell that surrounds the hexapole (15.2 cm total length) starting 2.5 cm from the inlet was added to the ESI/IF/6P source. Various pressures of nitrogen gas were added to the cell to alter the thermalization conditions, but no changes in the cross sections for $Co^{2+}(H_2O)_x$, where x = 5 and 6, were observed.

The ions generated and thermalized in the source were extracted from the hexapole ion guide and focused into a magnetic sector momentum analyzer for mass selection of the reactant ion. These reactant ions were then decelerated to a known kinetic energy and injected into an rf octopole ion guide³¹ where the ions were trapped radially and passed through a collision gas cell

containing Xe at varying pressures (0.05 - 0.20 mTorr). The pressures are low enough that single collision conditions dominate. Xenon was used as the collision gas to induce dissociation because it is heavy, monoatomic, polarizable, and chemically unreactive, all of which increase the efficiency of the transfer of kinetic energy to internal modes.³²⁻³⁴ After collision, product ions and remaining reactant ions drifted to the end of the octopole where they were extracted, mass analyzed using a quadrupole mass filter, and detected using a Daly detector.³⁵

Data Analysis. Ion intensities were converted to absolute cross sections using a Beer-Lambert law analogue, as described in detail elsewhere, with an uncertainty of \pm 20% (10% uncertainties each in pressure measurement and collision cell length). The laboratory ion potential, V_{lab} , was converted to the relative kinetic energy in the center-of-mass (CM) frame by $E_{CM} = E_{lab} \times m/(m+M)$, where $E_{lab} = 2V_{lab}$ because the ions are doubly charged, m is the mass of the neutral collision gas, and M is the mass of the reactant ion. The absolute zero of energy and the kinetic energy distribution of the ion beam were determined using a retarding potential technique, in which the derivative of the normalized ion intensity was fit to a Gaussian distribution (~0.12 eV FWHM). All energies below are reported in CM frame, unless noted otherwise.

To produce accurate thermochemical data from the modeling of the CID process, several effects must be considered: multiple collisions, lifetime effects, and energy distributions. To ensure rigorous single collision conditions, cross sections were obtained at multiple Xe pressures, about 0.20, 0.10, and 0.05 mTorr, and linearly extrapolated to zero pressure cross sections. The zero-pressure extrapolated cross sections for loss of a single ligand were modeled using the empirical threshold model shown in eq 3:

$$\sigma_{j}(E) = \sigma_{0,j} \sum_{i} g_{i} (E + E_{i} - E_{0,j})^{n} / E$$
(3)

where σ_0 is an energy independent scaling factor for channel j, E is the relative translational energy of the reactants, $E_{0,j}$ is the reaction threshold for channel j at 0 K, and n is an adjustable fitting parameter that describes the efficiency of the energy transfer upon collision.²¹ The summation is over the ro-vibrational states of the reactants with excitation energies, E_i , and populations, g_i ,

where $\Sigma g_i = 1$. The number of ro-vibrational states was directly counted by the Beyer–Swinehart–Stein–Rabinovich algorithm to evaluate the internal energy distribution for the reactants.³⁸⁻⁴¹ A Maxwell-Boltzmann distribution at 300 K was used to compute the relative populations, g_i . The number of accessible ro-vibrational states increases as the size of the reactant ions increases, such that those with energy in excess of the dissociation threshold may not have time to dissociate on the time scale of the experiment, $\tau \approx 5 \times 10^{-4}$ s.²¹ This can lead to a kinetic shift in the energy threshold, which can be accounted for by incorporating Rice–Ramsperger–Kassel–Marcus (RRKM) statistical theory⁴¹⁻⁴³ for unimolecular dissociation into eq 3, as shown in eq 4.⁴⁴

$$\sigma_j(E) = \left(\frac{n\sigma_{0,j}}{E}\right) \sum_i g_i \int_{E_{0,j}-E_i}^E \left[\frac{k_j(E^*)}{k_{tot}(E^*)}\right] (E - \varepsilon)^{n-1} P_{D1} d(\varepsilon) \tag{4}$$

In eq 4, ε is the energy transferred into internal degrees of freedom of the reactant ion during collision, such that the energized molecule (EM) has an internal energy of $E^* = \varepsilon + E_i$, and $k_{tot}(E^*)$ is the total unimolecular dissociation rate coefficient. The rate coefficient was used to calculate a probability of dissociation, $P_{D1} = 1 - \exp[-k_{tot}(E^*)\tau]$. The RRKM unimolecular dissociation rate coefficient is defined by eq 5,

$$k_{tot}(E^*) = \sum_{i} k_i(E^*) = \sum_{i} d_i N_i^{\dagger} (E^* - E_{0,i}) / h \rho(E^*)$$
 (5)

where $k_j(E^*)$ is the rate coefficient for a single dissociation channel j, d_j is the reaction degeneracy calculated from the ratio of rotational symmetry numbers⁴¹ of the reactants and products of channel j, $N_j^{\dagger}(E^*-E_{0,j})$ is the sum of the ro-vibrational states of the transition state (TS) at an energy ($E^*-E_{0,j}$) above the threshold for channel j, and $\rho(E^*)$ is the density of ro-vibrational states for the EM at the energy available, E^* . When the rate of dissociation is much faster than the average experimental time scale, eq 4 reduces to eq 3. Eq 4 also accounts for the competition between multiple dissociation pathways using the $k_j(E^*)/k_{tot}(E^*)$ ratio.^{44, 45}

Cross sections for the first and second water losses were modeled by combining eq 4, the cross section of the primary dissociation product, with the probability for further dissociation given by eq 6,

$$P_{D2} = 1 - e^{-k_2(E_2^*)\tau} (6)$$

where E_2^* is the internal energy of the product ion undergoing sequential dissociation. This energy is determined by energy conservation, $E_2^* = E^* - E_{0,j} - T_1 - E_L$, where T_1 is the translational energy of the primary products and E_L is the internal energy of the neutral product. As discussed elsewhere, the distributions in these energies are assigned on the basis of statistical considerations. For the remainder of this paper, representation of this sequential dissociation model that combines eqs 4 and 6 will be notated as eq 4 × 6. The bond dissociation energy (BDE) for the $Co^{2+}(H_2O)_{x-1}$ complex is the difference between the thresholds of these two product cross sections.

Calculation of the RRKM unimolecular rate coefficients requires the ro-vibrational states of the EM and TS. The molecular parameters for the EM were taken from quantum chemical calculations of the reactant ion. Water loss from a metal cation species, reaction 1, is a heterolytic bond cleavage with all the charge remaining on the cobalt containing fragment complex. As such these TSs were assumed to be loose with no reverse activation barrier⁴⁷ and were treated in the phase space limit (PSL), such that it used molecular parameters taken from quantum chemical calculations of the products. He Because the charge separation processes 2 produce two singly charged species, there must be an associated Coulomb barrier along the reaction coordinate for this dissociation channel such that the charge separation TSs are tight. The rate-limiting TSs for charge separation are labeled according to the products formed in reaction 2, i.e., TS[m + (x - m - 1)] where m is the number of waters attached to the CoOH+ product and (x - m - 1) is the number of waters attached to the H+ product. Molecular parameters for these TSs were taken directly from the calculations described below.

The CID cross sections of eq 4 and eq 4 × 6 were convoluted over the relative kinetic energy distributions of the $Co^{2+}(H_2O)_x$ and Xe reactants for comparison with the experimental cross sections.²⁰ A nonlinear least-squares fitting procedure was used to optimize the fitting parameters in each model. The uncertainties associated with the fitting parameters, $\sigma_{0,j}$, n, and $E_{0,j}$, were determined from modeling multiple data sets (at least eight zero pressure extrapolated cross sections for each system) and additional modeling of the cross sections by scaling the vibrational frequencies by $\pm 10\%$, varying the best fit n value by ± 0.1 , scaling the experimental time-of-flight up and down by a factor of 2, and including the absolute uncertainty of the energy scale, 0.05 eV (Lab). Because all sources of energy are accounted for in these analyses, the measured thresholds, $E_{0,j}$, equal the BDE at 0 K for the $Co^{2+}(H_2O)_x$ complex dissociating as in reaction 1^{48} or the height of the charge separation barrier of reaction 2.

Computational Details. Possible geometries for $Co^{2+}(H_2O)_x$ complexes were taken from previously examined geometries of Zn²⁺(H₂O)_x complexes,⁴ which were determined using a simulated annealing procedure that combines annealing cycles and ab initio calculations in order to thoroughly explore conformational space.⁴⁹ Notably the accuracy of the geometries for the Zn²⁺ complexes was confirmed by an independent infrared photodissociation spectroscopy study.²⁹ Additional structures of some larger complexes were explored by manually generating the initial geometry and following the procedure outlined below. Geometry optimizations for multiple isomers of the $Co^{2+}(H_2O)_x$ system were performed at the B3LYP/6-31G(d) level of theory^{50, 51} for inner shell sizes of 4, 5, and 6 at each x. The optimizations were refined at a B3LYP/6-311+G(d,p)level, which was used for the final geometry optimizations and to provide vibrational frequencies and rotational constants for the data analysis. Geometry optimizations utilizing empirical dispersion corrections were also determined at the B3LYP-GD3BJ/6-311+G(d,p) level.⁵² Calculations using B3LYP with and without dispersion corrections were both explored as the latter is still in widespread use and the present thermochemical results provide benchmark data for evaluating the accuracy of the dispersion corrections (which potentially overestimate dispersion). Single point energy calculations using the B3LYP/6-311+G(d,p) optimized geometries were

performed at B3LYP, B3P86,⁵³ and MP2(full)⁵⁴ (where full indicates correlation of all electrons) levels of theory using a 6-311+G(2d,2p) basis set and also at the B3LYP-GD3BJ/6-311+G(2d,2p)//B3LYP-GD3BJ/6-311+G(d,p) level. For brevity, these levels of theory will simply be referred to as B3LYP, B3P86, MP2, and B3LYP-GD3BJ throughout the rest of the paper.

Vibrational frequencies were scaled by 0.989⁵⁵ before being used in the modeling process and to calculate zero point energies to yield 0 K values as well as thermal corrections to 298 K. Basis set superposition errors (BSSE) were calculated for dissociation of the lowest energy structures at each level of theory in the full counterpoise (cp) limit.^{56, 57}

RESULTS

Collision-Induced Dissociation Cross-Sections of $Co^{2+}(H_2O)_x$. Experimental cross-sections for the collision-induced dissociation with Xe were acquired for $Co^{2+}(H_2O)_x$, x = 5 - 11, and are shown in Figure 1. In all cases, the loss of a single water molecule, reaction 1, is the dominant pathway, followed by the sequential loss of additional water molecules as the kinetic energy increases. In all cases, the total cross sections reach a magnitude that increases with x, consistent with gradually increasing complex sizes. Furthermore, the extended plateau in the total cross sections is evidence for sequential dissociation processes. Notably, the cross section for x = 5 is substantially smaller than that for x = 6 and smaller than the cross sections for the analogous Fe^{2+} and $Fe^{2+}(H_2O)_5$ system, an isobaric contaminant could explain the smaller cross section, although CID does not reveal the presence of another species.

As seen in Figure 1(a) and (b), for x = 11 and 10, respectively, cross sections for losses of up to six water ligands each were characterized. In addition, products corresponding to charge separation (CS) processes, reaction 2, were observed for x = 10. It can be seen that the CoOH⁺(H₂O)₃ and H⁺(H₂O)₃ products rise from similar thresholds, meaning that these species must come from dissociation of the Co²⁺(H₂O)₇ product in reaction 7.

$$Co^{2+}(H_2O)_7 \to CoOH^+(H_2O)_3 + H^+(H_2O)_3$$
 (7)

The apparent threshold for this CS reaction clearly exceeds that for loss of a water molecule from the x = 7 complex to form $Co^{2+}(H_2O)_6$, which explains why the CS cross section is so much smaller and rises less sharply than the cross section for water loss. It is also useful to recognize that the CS processes are entropically disfavored as they must pass over a rate-limiting TS corresponding to bringing the two incipient singly charged product ions together over a Coulombic barrier, whereas water loss processes always involve loose TSs. The cross section for $H^+(H_2O)_2$ rises with a similar magnitude as the $CoOH^+(H_2O)_3$ at a somewhat higher threshold than $H^+(H_2O)_3$. The apparent threshold of the $H^+(H_2O)_2$ product is much lower than that expected for sequential loss of water from $H^+(H_2O)_3$, where the BDE for $H^+(H_2O)_2$ - H_2O is 0.86 ± 0.06 eV. ⁴⁸ Thus, the $H^+(H_2O)_2$ must come from the dissociation of the $Co^{2+}(H_2O)_6$ product in reaction 8.

$$Co^{2+}(H_2O)_6 \rightarrow CoOH^+(H_2O)_3 + H^+(H_2O)_2$$
 (8)

The apparent thresholds for reaction 8 and that for loss of a water molecule to form $Co^{2+}(H_2O)_5$ are more similar with the apparent CS threshold ~0.4 eV higher.

For CID of x = 9 and 8, Figure 1(c) and (d), sequential loss of water ligands down to $Co^{2+}(H_2O)_4$ and the CS products found in reactions 7 and 8 were again characterized. It is now apparent that the magnitude of the $H^+(H_2O)_3$ cross section is smaller than those for $CoOH^+(H_2O)_3$ and $H^+(H_2O)_2$. Onsets of these CS reactions relative to H_2O loss products remain similar to those described for the x = 10 complex. Figure 1(e) shows the CID of $Co^{2+}(H_2O)_7$ follows the same product pathways as $Co^{2+}(H_2O)_8$, exhibiting the loss of four water ligands, although the cross section for $Co^{2+}(H_2O)_3$ is quite small. The CS products are also similar to those for x = 8 - 10, but now $CoOH^+(H_2O)_2$ and H^+H_2O are also observed at higher energies, starting near 1.5 and 3.0 eV, respectively. Indeed, the threshold for $CoOH^+(H_2O)_2$ relative to that for $CoOH^+(H_2O)_3$ in Figure 1(e) is comparable to the BDE for $CoOH^+(H_2O)_2$ -H₂O measured previously as 1.12 ± 0.07 eV. As such, the $CoOH^+(H_2O)_2$ product at its threshold is a result of sequential loss of water from

CoOH⁺(H₂O)₃ and its cross section exhibits evidence of contributions from the CoOH⁺(H₂O)₃ precursors formed in both reactions 7 and 8. At higher energies (above about 3 eV), the CoOH⁺(H₂O)₂ cross section increases, paralleling the onset in the H⁺H₂O cross section. This observation suggests that CS reaction 9 is occurring.

$$Co^{2+}(H_2O)_4 \to CoOH^+(H_2O)_2 + H^+H_2O$$
 (9)

If so, it can be seen that the apparent threshold for the H⁺H₂O product from CS reaction 9 is similar in both threshold energy and magnitude to that for formation of Co²⁺(H₂O)₃, Figure 1(e), suggesting these are competitive dissociation pathways of the Co²⁺(H₂O)₄ product. The CS reaction 9 has previously been identified in the photodissociation of Co²⁺(H₂O)₄ by Metz and coworkers.⁵⁸ They found that simple water loss was at least an order of magnitude less probable, which differs from the very similar probabilities of the two pathways observed here. This difference may simply be attributable to the differing activation methods. In addition, Kebarle and coworkers^{12, 16, 17} used high pressure mass spectrometry (HPMS) to observe CoOH⁺(H₂O)₂, CoOH⁺(H₂O), and H⁺H₂O, assigning these observations to reaction 9, although there is nothing in this work that allows them to definitively link the products observed as coming from the same reaction.

The presence of reaction 8 is confirmed by the results for Co²⁺(H₂O)₆, Figure 1(f), which can no longer dissociate by reaction 7. Now the H⁺(H₂O)₃ product is no longer observed and the cross sections for CoOH⁺(H₂O)₃ and H⁺(H₂O)₂ have similar energy dependences. Further, the sum of the CoOH⁺(H₂O)₃ and CoOH⁺(H₂O)₂ cross sections matches that of the sum of H⁺(H₂O)₂ and H⁺H₂O in shape, consistent with sequential loss of water ligands from the former to produce the latter at their thresholds. Relative thresholds are also consistent with this conclusion. The magnitudes of these two sums differ by approximately 50%. We have previously demonstrated that this can occur because the products of CS reactions have appreciable kinetic energy that is released once they pass over the Coulombic barrier.⁵ Momentum conservation dictates that the lighter products have a higher kinetic energy, such that they are less efficiently collected and

detected. Reaction 9 is also more easily observed in Figure 1(f) as a large increase in the CoOH⁺(H₂O)₂ and H⁺H₂O cross sections compared to those for CoOH⁺(H₂O)₃ and H⁺(H₂O)₂ (very evident on a linear cross section scale). Again, these cross sections follow a similar energy dependence and magnitude as formation of Co²⁺(H₂O)₃.

Unexpectedly, the dissociation of $Co^{2+}(H_2O)_5$, Figure 1(g), exhibits only loss of water ligands and no CS reactions were observed from x = 5. The failure to observe a CS reaction from $Co^{2+}(H_2O)_5$ is consistent with no evidence for such a reaction in the larger complexes. In contrast, on the basis of the results described above for dissociation of the x = 7 and 6 complexes, one might have expected to observe $CoOH^+(H_2O)_2$ and H^+H_2O products of reaction 9 with cross section magnitudes similar to that of the $Co^{2+}(H_2O)_3$ product. These products were specifically looked for but never seen with intensity above the signal-to-noise level ($\sim 0.01 \text{ Å}^2$). At this point in time, we have no ready explanation for the failure to observe reaction 9 in Figure 1(g) although this result is discussed further below.

Overview of Theoretical Results. Relative energies at 0 and 298 K of $Co^{2+}(H_2O)_x$ (x = 4 – 11) complexes calculated at different levels of theory are given in Table 1, with geometries of ground structures (GSs) shown in Figure 2. Table 1 reports relative energetics at 0 and 298 K for distinct low energy isomers of x = 4 - 11 complexes. Structures and relative energies at 0 and 298 K of all investigated isomers of $Co^{2+}(H_2O)_x$ are given in Table S1 of the Supplementary Information. Tables S2 and S3 provide electronic energies for all complexes investigated here. For all complexes, the quartet spin state of the $3d^7$ configuration on cobalt was found to be much more favorable energetically (by over 1.0 eV) compared to a doublet or sextet spin state.

We use an (x,y,z) nomenclature to describe the number of water molecules in the first (x), second (y), and third (z) solvent shells of each unique structure. To describe the hydrogen bonding of waters in the cluster, isomers are further denoted using an A/D nomenclature where a water molecule can be a single (A) or double (AA) hydrogen bond acceptor and/or single (D) or double (DD) hydrogen bond donor with shells separated by an underscore (_).To further distinguish between structures with similar bonding schemes but differing geometric parameters, additions to

the nomenclature may include: point group symmetries; the subscripts "a" or "b" to indicate if the bond connects to an axial or base ligand, respectively; series of oxygen – cobalt dication –oxygen angles denoted as subscript "g" (gauche) for angles between 45° and 135° and "t" (trans) for angles >135°.

Theoretical Geometries for $Co^{2+}(H_2O)_x$ Ground Structures. As seen in Table 1, there is a discrepancy among the different levels of theory as to the coordination number (CN), the number of ligands that directly bind to the metal and form the first solvent shell, for $Co^{2+}(H_2O)_x$. The progression of the GS solvent shell growth at the different CNs are displayed in Figure 2. The B3LYP and B3P86 levels predict that CN = 4 for x = 4 - 7, and then CN = 5 for $x \ge 8$ at 0 and 298 K. MP2 predicts four-coordinate GSs for x = 4 and 5 and then CN = 6 for $x \ge 6$ at 0 and 298 K. Temperature becomes a factor for B3LYP-GD3BJ. For x = 4 - 8, the B3LYP-GD3BJ 298 K GSs are the same as B3LYP and B3P86, whereas the 0 K GSs agree with MP2 GSs. At x = 9 - 11, the B3LYP-GD3BJ GSs are CN = 6 at both 0 and 298 K GS, agreeing with MP2.

All levels of theory predict GSs with four waters directly binding to Co^{2+} for x = 4 and 5 (Table 1). The (4,0) $Co^{2+}(H_2O)_4$ GS isomer exhibits a distorted tetrahedral geometry with $\angle O$ -Co-O of 105° and 112° and four Co-O bond lengths of 2.012 Å. The nonsymmetrical orientation of the water ligands results from their participation in long-range hydrogen bonding interactions (~3.6 Å between H and O). The x = 5 GS, (4,1)_AA, is the (4,0) isomer with addition of the fifth water ligand promoted to a second solvent shell by accepting hydrogen bonds from two inner shell waters. Table 1 shows the (5,0) isomer is 17 - 26 kJ/mol higher in 298 K energy than the (4,1) GS. These four-coordinate structures are similar to those predicted and identified spectroscopically for $CoOH^+(H_2O)_3$, 8 , 59 where the $CoOH^+(H_2O)_3$ GS complex had three water ligands and the hydroxide bound directly to the cobalt ion. The fourth water ligand in $CoOH^+(H_2O)_4$ was also promoted into the second solvent shell where it accepted a single hydrogen bond from an inner shell water and donated a hydrogen bond to the inner shell hydroxide. It can be realized that in both the Co^{2+} and $CoOH^+$ complexes the metal ion has a $3d^7$ electron

configuration such that a tetrahedral geometry is favored, as this gives an orbital occupation of $(e)^4(t_2)^3$ for a quartet spin state.

At Co2+(H2O)6, levels of theory diverge for predicting the lowest energy isomer. The B3LYP, B3P86, and B3LYP-GD3BJ (298 K) levels of theory continue to predict a four-water inner solvent shell GS with the (4,2) 4D 2AA isomer. This isomer has the sixth water ligand accepting hydrogen bonds from two inner shell water ligands of the (4,1) AA complex, such that the two second solvent shell water molecules are opposite each other. MP2 and B3LYP-GD3BJ (0 K) predict the lowest energy x = 6 isomer to be the six-coordinate (6,0) complex, where all six water molecules directly interact with the metal center in a tetragonally distorted octahedral geometry with Co – O bond lengths of 2.126 Å (4) and 2.128 Å (2). In the (6,0) complex, the orientations of the ligands are again determined by long (3.0 - 3.1 Å) inter-ligand hydrogen bonding occurring between the hydrogen atom of one ligand and the oxygen atom of a neighboring water unit (Figure 2) such that the symmetry is D_{2h} . The Co – O bond lengths determined here are ~0.016 Å shorter than predicted by Akesson et al. 60 using MCSCF methods for their (6,0) complex with T_h symmetry (where all Co-O bond lengths are equal and the hydrogen bonding dictates the high symmetry), predicted here to be 11 - 18 kJ/mol higher in relative 298 K energy than the GS (Table S1). Note that the six-coordinate geometry has an orbital occupation of $(t_{2g})^5(e_g)^2$ for a quartet spin state, such that a Jahn-Teller distortion from the octahedral T_h symmetry is expected.

Theory also predicts both four- and six-coordinate GSs at x = 7, Figure 2. B3LYP, B3P86, and B3LYP-GD3BJ (298 K) levels predict the lowest energy isomer of $Co^{2+}(H_2O)_7$ has a four-water inner shell structure, $(4,3)_3D$, DD_2AA , A which is similar to the $(4,2)_4D_2AA$ isomer where the third outer shell water accepts a single hydrogen bond from an inner shell water. The $(6,1)_AA$ is predicted by MP2(full) and B3LYP-GD3BJ (0 K) levels to be the lowest energy isomer. In this isomer, the seventh water is in the second solvent shell, doubly bound via two hydrogen bonds from neighboring inner-shell water ligands.

At Co²⁺(H₂O)₈, theory stops predicting a four-coordinate ground structure. Here, the B3LYP, B3P86 and B3LYP-GD3BJ (298 K) levels predict the lowest energy isomer to have a

five-water inner solvent shell, (5,3)_2D,2DD_3A_bA_b. Figure 2 shows this isomer has a distorted square pyramidal inner shell geometry with the three outer shell ligands adjacent to each other in the plane of the pyramid base. For MP2 and B3LYP-GD3BJ (0 K) levels, the (6,2)_4D_2AA_t isomer is predicted to be the GS. As shown in Figure 2, this structure has two second-shell water ligands doubly hydrogen bonded to the inner solvent shell opposite each other (t = trans).

The five-coordinate GS predicted by B3LYP and B3P86 levels for x = 9 is $(5,4)_2D,3DD_4AA$. This structure is similar in geometry to the x = 8 (5,3) GS but the eighth water accepts hydrogen bonds from two inner solvent waters, one in the axial position and one in the base. If all four second shell waters bind symmetrically to inner shell base waters, $(5,4)_4DD_4AA$, this isomer lies 0 - 2 kJ/mol higher in 298 K relative energy, Table S1. The six-coordinate GS predicted by MP2 and B3LYP-GD3BJ (0 and 298 K) is a $(6,3)_6D_3AA$ geometry with each of the six inner solvent shell waters donating only a single hydrogen bond to an outer solvent shell water. In this complex, the three second solvent shell water ligands bind in equivalent locations, Figure 2.

The two predicted lowest energy Co²⁺(H₂O)₁₀ complexes are shown in Figure 2. B3LYP and B3P86 levels predict the (5,5)_D,4DD_4AA,A geometry to be the GS. In this structure, four second solvent shell waters form two hydrogen bonds with the base of the square pyramidal inner solvent shell and the fifth second shell water accepts a single hydrogen bond from the axial inner solvent shell water. The (6,4)_4D,2DD_4AA isomer is predicted to be the MP2 and B3LYP-GD3BJ GS. This isomer has the outer shell waters oriented in such a way that two of the outer solvent shell water ligands are adjacent to each other with one inner solvent water shared between the two in the *xy* plane, while the other two outer shell water ligands are adjacent to each other with one inner solvent water shared between the two in the *xz* plane.

Figure 2 shows the three possible GSs for the $Co^{2+}(H_2O)_{11}$ complex, two five-coordinate and one six-coordinate, depending on the level of theory. B3LYP predicts the $(5,6)_5DD_4AA,2A$ isomer as the GS, similar in structure to the x = 10 (5,5) GS with the addition of another water ligand accepting a single hydrogen bond from the inner shell water ligand in the axial position.

B3P86 predicted a GS of (5,5,1)_D,4DD_A,3AA,AAD_A, which is also similar to the x = 10 (5,5) GS, with the eleventh water in a third solvent shell singly bound to a second solvent shell water in the base of the square pyramid. MP2 and B3LYP-GD3BJ continue to predict a six-coordinate GS with the (6,5)_2D,4DD_5AA structure where the five second shell waters are all adjacent to each other in different planes with four double donating (DD) inner shell waters shared between them.

In agreement with the MP2 and B3LYP-GD3BJ results predicting CN = 6, Gilson and Krauss⁶¹ used CAS-MCSCF and MCQDPT calculations to interpret the absorption spectrum of aqueous Co²⁺ and found that the dominant species in solution is six-coordinate with some evidence of five-coordinate species. Metz and coworkers⁵⁸ reported that their photodissociation spectrum of $Co^{2+}(H_2O)_6$ was only consistent with the (6,0) structure, which suggests that the relative energies predicted by MP2 are more accurate than the other methods explored here. This conclusion is consistent with previous infrared photon dissociation (IRPD) spectroscopy experiments of $Zn^{2+}(H_2O)_x$, x = 6 - 12, where the MP2(full)/6-311+G(2d,2p)//B3LYP/6-311+G(d,p) level of theory gave good agreement with experiment whereas B3LYP and B3P86 levels did not.

Theoretical Geometries for Charge Separation Transition States. The transition states for the charge separation reactions 7-9 involve the heterolytic cleavage of an O-H bond leading to the incipient products, $CoOH^+(H_2O)_m$ and $H^+(H_2O)_{x-m-1}$. Molecular parameters for these rate-limiting TSs are needed for thermochemical analysis. Optimized geometries of these tight TSs are shown in Figure 3 and include possible pathways for CS reactions of $Co^{2+}(H_2O)_5$ as well (both TS[3+1] and TS[2+2]). The $(O-H^+)$ distances between the hydroxide oxygen and leaving proton in these TSs is generally near 3.2 Å, although TS[2+2] has an O-H⁺ distance of only 2.94 Å. Such variations in these TS geometries have been observed previously for the analogous complexes of Fe^{2+} and Ni^{2+} .^{1,2}

Thermochemical Results. Primary and secondary dissociation product cross sections for all $Co^{2+}(H_2O)_x$ complexes observed were modeled in several ways, with average optimum modeling parameters obtained listed in Table 2. It can be seen that the σ_0 values generally match the absolute magnitudes of the cross sections being modeled, with small variations that are tied to

the influence of the n and E_0 parameters on the model. All complexes are believed to be thermally equilibrated in the source, such that the modeling assumes the reactant isomers are the 298 K GS with an internal energy distribution of 298 K. The product isomer is assigned as the 0 K GS because previous studies have found that our threshold analyses are dominated by the lowest energy 0 K enthalpy species.^{1, 4} Threshold E_0 values were determined for the primary dissociation of each complex from modeling with (eq 4) and without (eq 3) including RRKM theory, which takes lifetime effects into account. The primary threshold values without lifetime effects are higher because of a kinetic shift, which increases as the complexes get larger (from 0.1 eV for x = 5 to 0.6 eV for x = 11) because of the increased dissociation lifetime. Table 2 also includes values of the entropies of activation, $\Delta S^{\dagger}_{1000}$, which represent the measure of looseness of the transition states. All of these values are positive, consistent with a loose PSL TS.

The predicted GSs differ for the x = 6 - 11 complexes depending on the level of theory, and in several cases, there are low-energy isomers at 298 K energies such that multiple isomers could be present in the source. In these cases, the data were modeled using each of these possible isomers individually, Table 2. Changes in the reaction thresholds are a consequence of differences in the kinetic shifts of the model. This becomes more evident for reactant complexes with more outer shell waters and more single hydrogen bound waters (A) with low torsional frequencies that lead to a higher density of states, lowering the rate of dissociation, thereby increasing the kinetic shift and lowering the 0 K reaction threshold.⁴ Consequently, we observed very minimal changes in the reaction thresholds when the data were modeled using different CN assumptions, with differences of only 0.01 - 0.03 eV for x = 6 - 11, where isomers with higher densities of states (CN = 4 and 5) have lower thresholds than CN = 6.

In general, as the complex size increases from $\text{Co}^{2+}(\text{H}_2\text{O})_6$ to $\text{Co}^{2+}(\text{H}_2\text{O})_{11}$, reaction thresholds for loss of a single water molecule decrease. The largest decrease in consecutive E_0 values is 0.31-0.33 eV for the x=6 to x=7 complexes. This large change is potentially consistent with the onset of the second solvent shell and evidence for the $(6,0) \rightarrow (6,1)$ isomers (MP2 and B3LYP-GD3BJ) as opposed to the $(4,2) \rightarrow (4,3)$ (B3LYP and B3P86). Uncharacteristically, the

measured BDEs increase by 0.09 eV for x = 5 to 6. We attribute this increase to a change from (4,1) with a weakly bound second solvent shell water ligand to (6,0), where all ligands bind directly to the cobalt ion. Again, this increase is consistent with geometries predicted by MP2 and B3LYP-GD3BJ (0 K), but not for B3LYP, B3P86, and B3LYP-GD3BJ (298 K), which suggest geometries of (4,1) and (4,2). Because MP2 theory predicts several aspects of this thermochemistry more correctly, additional thermochemical analysis below is based on the GS structures predicted by the MP2 energetics.

Thermochemical Results for Competitive Water Loss Versus Charge Separation. For the Co²⁺(H₂O)₆ and Co²⁺(H₂O)₇ complexes, water loss and charge separation processes are competitive primary dissociation pathways, Figure 1 (e) and (f), respectively. These dissociative pathways are modeled simultaneously using eq 4 with optimum modeling parameters also included in Table 2. The primary water loss thresholds are essentially unaffected by including competition with the CS products. Competitive analysis of the x = 6 CID cross sections (assuming a (6,0)reactant) measures a dissociation threshold for H_2O loss of 1.11 ± 0.07 eV and a threshold for TS[3+2] of 0.97 ± 0.06 eV. The CS dissociation pathway is energetically favored by 0.14 ± 0.04 eV over the water loss channel and they have similar entropies of activation. These results help explain why the relative magnitudes of the two pathways differ by only about an order of magnitude, Figure 1(f). For competitive analysis of the x = 7 dissociation cross sections (assuming a (6,1) AA reactant), H₂O loss is measured as 0.80 ± 0.08 eV and the threshold for TS[3+3] is 0.82 ± 0.10 eV, with a difference of only 0.02 ± 0.03 eV. Loss of H₂O is energetically and entropically more favorable at x = 7 with its lower threshold for dissociation and larger $\Delta S^{\dagger}_{1000}$ value. As a consequence, here the water loss channel is favored by about two orders of magnitude compared to the competing CS reaction pathway, Figure 1(e).

Thermochemical Results for Sequential Dissociation. Thermochemical results for the secondary water loss thresholds using the sequential model for analysis are also reported in Table 2. The sequential secondary water losses were modeled by simultaneously analyzing the primary and secondary dissociation product cross sections using eqs 4 and 4×6 , where the difference

between the primary and secondary thresholds is used to calculate an independent measurement for the bond dissociation energy for $Co^{2+}(H_2O)_{x-1}$ dissociating to $Co^{2+}(H_2O)_{x-2} + H_2O$. This difference in thresholds can be measured with more precision than the absolute values for each threshold because many systematic sources of uncertainty cancel; however, their accuracy can suffer from the additional assumptions needed in the modeling. Figure 4 shows the sequential analysis of primary and secondary cross sections for x = 8 as well as the model of the total cross section. Figure 4 shows the sequential analysis reproduces both product cross sections and their total well over extended magnitude and energy ranges ($\sim 2.5 \text{ eV}$). Direct comparison of the models for the total cross sections versus the sequential models of the primary cross sections show that the analogous σ_0 , n, and E_0 values are nearly identical with the threshold values within 0.06 eV in all cases. Thus, threshold energies for the primary water loss channels are basically unaffected by consideration of the secondary loss channel.

The sequential dissociation at x = 6 is modeled as a $(6,0) \rightarrow (4,1) + H_2O \rightarrow (4,0) + 2$ H₂O process; however, the primary dissociation to form the (4,1) product is complicated by competition with the CS process, reaction 8. Analyzing this sequential process including competition, Figure 5, we measure thresholds of 1.08 ± 0.07 eV and 2.22 ± 0.09 eV for the first and second water losses, respectively. The difference between thresholds, 1.13 eV ± 0.08 eV, gives the sequential BDE for Co²⁺(H₂O)₄-H₂O, which is within combined experimental uncertainty of the threshold for single water loss from Co²⁺(H₂O)₅, 1.02 ± 0.07 eV. Similarly, sequential modeling of the x = 7 reactant of the CS reaction 7 gives a sequential BDE of 1.13 ± 0.06 eV, which is in excellent agreement with the primary dissociation threshold of 1.11 ± 0.08 eV determined for x = 6.

Comparison of Experimental and Theoretical Bond Enthalpies. Primary and secondary experimental 0 K hydration enthalpies for the loss of water from $Co^{2+}(H_2O)_x$ (x = 5 - 11) complexes are compared in Table 3. As discussed above, there is evidence that our most accurate interpretations of the data are from the relative energies and GSs predicted at the MP2 level of theory. Therefore, only the BDEs from the MP2 predicted GSs are given in Table 3 (although alternative interpretations give very similar values, within 3 kJ/mol). Secondary bond enthalpies

(obtained from differences between the primary and secondary thresholds) are systematically higher than the values obtained from the corresponding primary thresholds, but agree fairly well. Specifically, the secondary BDE for x = 5 agrees within 10 kJ/mol of the primary value, the x = 6 – 9 secondary BDEs are similar to the primary values (less than 7 kJ/mol difference), and the largest complex studied, x = 10, has primary and secondary BDEs that differ by a larger amount of 14 kJ/mol. Overall, the mean absolute deviation between the primary and secondary values is 7.9 kJ/mol, comparable to the mean experimental uncertainties of either value.

Table 3 also includes theoretical 0 K hydration bond enthalpies for the loss of water from $\text{Co}^{2+}(\text{H}_2\text{O})_x$ (x = 1 - 11) complexes with and without cp corrections. Our experimental values agree well with calculated 0 K hydration enthalpies at all levels of theory considered here, with MADs of 9 – 14 kJ/mol for primary BDEs and 7 – 9 kJ/mol for secondary BDEs, Table 3. When cp corrections are not included, agreement is worsened by 2 - 8 kJ/mol for primary BDEs. Interestingly, Table 3 shows the addition of empirical dispersion forces to B3LYP degrades the agreement with experiment by ~5 kJ/mol. Figure 6 graphically compares the primary and secondary experimental $Co^{2+}(H_2O)_x$ BDEs for x = 4 - 11 with theoretical values. BDEs decrease very sharply from x = 4 to 5, attributed above to putting the fifth ligand in the second solvent shell. The increase in BDEs from x = 5 and 6 results from putting all ligands back into the first solvent shell of the (6,0) complex. This leads to a relatively large decrease from x=6 to 7, which again involves addition to the second solvent shell. The almost linear trend for x = 7 - 10 emphasizes no changes in coordination number over this range of complex sizes. Figure 6 shows that MP2 predicts a slightly larger decrease in BDEs from x = 6 to 7 compared to that experimentally observed and a significantly larger decrease compared to the DFT levels, which do not predict a solvent shell growth here. MP2 results also predict a small increase in BDEs from x = 7 and 8, whereas experiment and DFT results show decreases. This difference is attributed to MP2 being more sensitive to long range hydrogen bonding. Here attachment of the second shell ligand in the (6,1) AA complex perturbs the network of these interactions established in (6,0), Figure 2. Addition of the eighth water takes advantage of the already perturbed network such that the (6,2) GS has a larger BDE.

For larger complexes, x = 9 - 11, theoretical results overestimate experimental results by 13 - 26 kJ/mol. Similar discrepancies between theoretical and experimental BDEs for the larger x complexes (≥ 9) have been observed for other hydrated transition metal ions. 1,2,4,5 It is possible that the discrepancy indicates that our ion source generates distributions of low-energy isomers for these larger x complexes or that they are incompletely thermalized because of the weakly bound outer shell water ligands. In either case, primary dissociation thresholds would be lower than the BDE for the GS, whereas secondary dissociation thresholds would potentially be more accurate as both the primary and secondary water loss thresholds would be shifted by the same amount. Alternatively, these discrepancies could be a result of theory not correctly describing the outer shell water binding. Investigation of this latter possibility using more advanced computational approaches would be welcome.

Comparison to Fe²⁺ and Ni²⁺ Hydration Enthalpies. Figure 7 compares the experimental 0 K bond enthalpies for Co²⁺(H₂O)_x (3d⁷) with those previously determined for Fe²⁺(H₂O)_x (3d⁶)¹ and Ni²⁺(H₂O)_x (3d⁸),² to highlight the trends for each value of x where x = 4 - 11. Figure 7 illustrates that the BDEs for larger complexes ($x \ge 7$) are essentially equivalent, within experimental uncertainty of each other. This trend is not unexpected as all three metals are predicted to have similar octahedral inner-shell GSs for $x \ge 6$ with similar second solvent shell growth. Thus, the BDEs for all three metals at the large x values are governed by loss of a water accepting hydrogen bonds from one or two inner shell waters. An interesting diversion from this similarity of BDEs occurs at x = 5 and 6. For x = 5, the BDE for Co²⁺ is lower than that of Fe²⁺, which is lower than that of Ni²⁺, whereas values for x = 6 increase steadily from Fe²⁺ to Co²⁺ to Ni²⁺. The latter changes can be assigned to the expected trend for (6,0) complexes as the metal dication gets smaller (because of the increasing nuclear charge as one moves across the periodic table), 0.78 to 0.75 to 0.69 Å for Fe²⁺ to Co²⁺ to Ni²⁺, respectively.⁶² The very different trend for x = 5 can be attributed to the differing coordination numbers of the different metals, as iron and

nickel have all five water ligands directly bound to the metal ion in (5,0) GSs and follow the same increasing BDE trend exhibited for x = 6. In contrast, for cobalt, the fifth water is more weakly bound in the second solvent shell in a (4,1) GS.

At x = 4, all geometries are predicted to be (4,0), but the BDEs do not follow the nuclear charge trend seen for x = 6 because the geometries are actually distinct. For Ni²⁺ (3d⁸), calculations showed that the triplet state (4,0) GS has a see-saw geometry with singly occupied molecular orbitals (SOMOs) in octahedral-like e_g MOs.² For Co²⁺ (3d⁷), the quartet state (4,0) GS SOMOs are the three tetrahedral t_2 MOs, in agreement with that found for the (3,1) GS of CoOH⁺(H₂O)₄.⁸ Thus, the Co²⁺ (4,0) GS has a distorted tetrahedral molecular geometry with \angle O-Co-O of 105° and 112°. This scheme is similar for Fe²⁺ (3d⁶), where the quintet state (4,0) GS also exhibits distorted tetrahedral geometry, but distorts to a lesser degree than Co²⁺ with \angle O-Co-O of 108° and 110°. The distortion and increased ligand-ligand repulsion for Co²⁺ and to a greater extent for Ni²⁺ explain the decreasing BDE trend at x = 4.

Conversion of 0 K Hydration Energies to 298 K. In all cases, the threshold energies obtained including lifetime effects are assigned as the 0 K bond energies. A rigid rotor/harmonic oscillator (RR/HO) approximation using the vibrational frequencies (scaled by 0.989) and rotational constants calculated at the B3LYP/6-311+G(d,p) level of theory was used to calculate ΔH_{298} - ΔH_0 and $T\Delta S_{298}$ values for dissociation. These factors were used to convert the 0 K bond energies into 298 K bond enthalpies (ΔH_{298}) and to determine free energies (ΔG_{298}) of dissociation. These values are listed for $Co^{2+}(H_2O)_x$, x = 4 - 11 in Table 4. The uncertainties in these conversions were obtained by scaling the vibrational frequencies up and down by 10%. It should be noted that some of the low vibrational frequencies correspond to torsional motions of the water ligands and thus the RR/HO approximations may not be accurate. The 298 K hydration enthalpies (ΔH_{298}) track the trends from the 0 K hydration enthalpies (ΔH_0) discussed above. The free energies of dissociation (ΔG_{298}) decrease with increasing number of water ligands for all complexes observed. Note that the x = 11 free energy of dissociation is only 0.04 ± 10.9 kJ/mol, which indicates that at

room temperature its dissociation is nearly spontaneous. This explains why our source does not make larger clusters (with weaker hydration energies) efficiently.

Charge Separation: Energetic Barriers. Table 5 presents the predicted barrier heights for the charge separation processes of $Co^{2+}(H_2O)_x$, where x = 4 - 7, including reactions 7 - 9, and also compares the experimental and theoretical barrier heights of the charge separation pathways to the experimental and predicted energies for water loss dissociation pathways. The structures of each of the likely rate-limiting TSs are shown in Figure 3, and in each case correspond to heterolytic cleavage of an O-H bond. The dominant CS channel of Co²⁺(H₂O)₇ is CoOH⁺(H₂O)₃ + H⁺(H₂O)₃, reaction 7, which occurs through TS[3+3]. Theory finds that this barrier height is 60 – 94 kJ/mol, such that the B3LYP-GD3BJ value agrees best with the experimental value of 79 ± 9 kJ/mol. DFT levels of theory predict the TS[3+3] barrier to be lower in energy than the single water loss BDE by 4 - 23 kJ/mol; however, the MP2 level calculates water loss to be lower in energy than the TS[3+3] pathway by 28 kJ/mol, as shown in the simplified potential energy surface of Figure S1 of the Supplementary Information. Modeling the competitive channels determines the threshold for charge separation is indeed higher than that for water loss but by only 2 ± 3 kJ/mol (Table 5). This energetic difference is closest to that predicted by B3LYP-GD3BJ, however, the MP2(full) level best represents the enthalpic preference for water loss over CS as determined experimentally here. The predicted reverse Coulomb barriers for CoOH+(H2O)3 + H+(H2O)3 to TS[3+3] are nearly equivalent, 146 – 150 kJ/mol for the DFT levels of theory and slightly lower for MP2 at 139 kJ/mol. Note that the overall CS reaction 7 is strongly exothermic by 46 – 89 kJ/mol.

For x = 6, the dominant CS channel of CoOH⁺(H₂O)₃ + H⁺(H₂O)₂, reaction 8, occurs through TS[3+2] with predicted barrier heights of 66 - 117 kJ/mol. Again, the experimental value of 94 ± 6 kJ/mol agrees best with B3LYP-GD3BJ results, which also predicts the threshold for reaction 1 well. All levels of theory predict the barrier height of TS[3+2] to be lower in energy than the water loss BDE by 24 - 32 kJ/mol for DFT levels and 7 kJ/mol for MP2, as illustrated in Figure S2 of the Supplementary Information. Modeling of the data suggests that the threshold for

charge separation is 13 ± 4 kJ/mol lower in energy than that for water loss, most closely agreeing with the enthalpic predictions of the B3LYP-GD3BJ and MP2 levels. The predicted values for the reverse Coulomb barrier are nearly identical to those for x = 7, with values only ~ 1 kJ/mol higher. Again, the overall CS reaction is exothermic, here by 23 - 85 kJ/mol.

For x = 5, the predicted barrier heights for TS[2+2] (leading to CoOH⁺(H₂O)₂ + H⁺(H₂O)₂ products) range from 77 – 117 kJ/mol and 124 -142 kJ/mol for TS[3+1] (leading to CoOH⁺(H₂O)₃ + H⁺(H₂O) products). DFT levels of theory predict the TS[2+2] barrier to be lower in energy than the single water loss BDE by 23 – 31 kJ/mol; however, the MP2 level calculates TS[2+2] to be higher in energy by 9 kJ/mol. All levels of theory predict that the TS[3+1] barrier height to be higher in energy than water loss by 17 - 34 kJ/mol. These results and the MP2 results for TS[2+2] are consistent with no primary dissociative CS pathways being observed directly from the CID of x = 5. To investigate this further, a complete reaction coordinate for the decomposition of $Co^{2+}(H_2O)_5$ by water loss and charge separation to $CoOH^+(H_2O)_2 + H^+(H_2O)_2$ was investigated theoretically and is shown in Figure 8. Figure 8 shows the individual steps needed for the ground Co²⁺(H₂O)₅ (4,1) AA complex to rearrange to TS[2+2], which requires that one of the water ligands be in a third solvent shell, i.e., formation of a (3,1,1) complex. As can be seen in the figure, this first requires moving one of the water ligands bound to the metal into the second shell forming the (3,2) AA,A complex, which then rearranges to form (3,1,1) AAD A. Although this complex can conceivably dissociate directly to TS[2+2], the barrier to rearrange to (3,1,1) AD A is small and the latter complex is the obvious precursor to TS[2+2]. All of these steps are needed for dissociation to $CoOH^+(H_2O)_2 + H^+(H_2O)_2$. Comparison of the energies of these various transition states shows that the rate-limiting TS for this pathway may not be TS[2+2], but TS[(3,2)-(3,1,1)]where the second solvent shell water is promoted to the third solvent shell. Indeed, TS[(3,2)-(3,1,1)] is found to be higher in energy than TS[2+2] and water loss for all levels of theory (Table 5). Hence, all levels of theory agree that both charge separation processes available for the x = 5complex are enthalpically disfavored compared with water loss in reaction 1 by 2 – 5 kJ/mol at the DFT levels and 10 kJ/mol for MP2.

A reviewer wonders whether loss of water ligands from the intermediates accessed along the path towards charge separation, i.e., (3,2) and (3,1,1), needs to be considered as it might be more efficient than from the (4,1) ground isomer. It can be realized that the competition between the water loss and charge separation pathways according to eq 4 is governed by their respective rate-limiting transition states in the form of N_i^{\dagger} (eq 5), which are independent of the intermediates from which they evolve. Furthermore, one imagines that the "efficient" loss of water from the (3,2) and both (3,1,1) intermediates occurs by loss of the outermost water, which would generate the excited isomer of the products, Co⁺(H₂O)₄ (3,1) AA, rather than the (4,0) ground isomer. This means that such dissociation pathways will not be competitive at the threshold for water loss. Furthermore, it can be seen in Figure 8 that loss of the outermost water from the (3,1,1) intermediate will not be competitive with the charge separation pathway as loss of water to form the (3,1) complex is much higher in energy than the transition states leading to the CoOH⁺(H₂O)₂ $+ H^{+}(H_2O)_2$ products. It is true that water loss from the (3,2) and (3,1,1) intermediates to form the (4,0) ground product is faster than from the (4,1) reactant. This is a result of the much lower density of states of these intermediates compared to that of the ground reactant (denominator in eq 5), but the same acceleration of the charge separation channel also occurs. It can also be realized that the population of these high energy intermediates is limited because their density of states is much lower than that of the ground reactant, indeed by an extent that matches the expected acceleration in the rate. Similar considerations hold for all of the different reactant sizes. Any uncertainties that these factors might introduce should be well within those already included by the frequency variations to both the TS and EM, as noted above. Overall, we believe that the analysis conducted here of the rates of dissociation along both pathways are comprehensive within the scope of statistical rate theories.

The predicted barrier heights for the x = 4 rate-limiting TS[2+1] range from 126 - 157 kJ/mol, with a reverse barrier height predicted to be ~ 163 kJ/mol for DFT levels and 149 kJ/mol for MP2. The complete potential energy surface is shown in Figure S3 of the Supplementary Information and confirms that TS[2+1] is rate limiting. This particular system (x = 4) has been

examined theoretically before by Beyer and Metz, who obtained a TS[2+1] barrier height of 145 kJ/mol and a reverse barrier of 166 kJ/mol.⁶³ Compared to water loss, all levels of theory predict that the barrier height for TS[2+1] is 44 – 54 kJ/mol lower in energy than water loss. As *x* increases, the reverse Coulomb barriers increase for all levels of theory here, consistent with observations from previous studies of hydrated Fe²⁺, Ni²⁺, Zn²⁺, and Cd²⁺ systems.^{1, 2, 5, 7}

The theoretical conclusion that TS[2+1] lies below the energy for formation of Co²⁺(H₂O)₃ + H₂O is consistent with the observation of reaction 9 by Metz and coworkers⁵⁸ as well as observation of this process in the dissociation of the Co²⁺(H₂O)₆ complex here. The question remains why no signs of this reaction were observed for dissociation of Co²⁺(H₂O)₅, Figure 1(g). Notably, this complex could only be generated in the source in sufficient abundance for CID study by use of the in-source electrodes, with maximum ion signal at -17.0 V on the electrodes. It seems possible that these conditions perturb the behavior of the Co²⁺(H₂O)₅ complex formed, but this conclusion is not consistent with the reasonable thermochemistry that analysis of these data provided above. Further, as noted in the experimental section, additional experiments designed to test complete thermalization by adding nitrogen gas in a collision cell in the source region led to no changes in the observed behavior of either x = 5 or 6 complexes. A similar lack of CS pathways phenomenon was observed for Ni²⁺(H₂O)₄, in which larger complex sizes of x showed evidence for a CS pathway from x = 4, yet none were observed when this ion was selected as the reactant for CID. This observation was explained by a dynamical hypothesis that the second shell water ligand of (4,1) AA provides a larger collision cross section compared to a more compact structure, i.e. (5,0). Collisions at larger impact parameters with an outer shell water ligand will preferentially excite this ligand leading to direct water loss, whereas smaller impact parameters leading to more general vibrational excitation are needed for the system to explore the tight TSs leading to charge separation.

As discussed above and seen in Figure 1, the experimental cross sections show that charge separation occurs for $Co^{2+}(H_2O)_x$ complexes of x = 4, 6, and 7. From earlier definitions of critical size, we would assign the maximum x at which CS and water loss become competitive to be $x_{crit} = x_{crit} = x_{cri$

7. In contrast, modeling the competitive processes for x = 7 shows that the CS process is energetically disfavored over water loss. The largest value of x at which the charge separation is energetically favored over the loss of one water ligand for $Co^{2+}(H_2O)_x$ is $x_{crit} = 6$, as determined by modeling the competitive pathways of TS[3+2] and water loss. This assignment also agrees with theory where the barrier height for TS[3+2] is predicted to be lower than water loss by all levels of theory investigated here (Table 5). This x_{crit} value for Co^{2+} is greater than found by Kebarle and coworkers, $x_{crit} = 4$, $^{12, 16, 17}$ and Shvartzburg and Siu, $x_{crit} = 5$, although in both of these reports, their observations do not permit both partners in the charge separation pathways to be linked together, thereby prohibiting a definitive assignment. A value of $x_{crit} = 6$ would also explain the difficulty of generating smaller complex sizes, and potentially contribute to the lack of evidence of expected CS pathways at x = 5.

CONCLUSION

Complementing our previous transition metal dication hydration studies, $^{1-7}$ the kinetic energy dependent cross sections for collision-induced dissociation of $Co^{2+}(H_2O)_x$ complexes were determined using guided ion beam tandem mass spectrometry for x = 5 - 11. The dominant CID pathway for all values of x studied is the loss of a single water molecule from the reactant ion. The data were analyzed to yield primary and secondary bond dissociation energies (BDEs) for the loss of one or two ligands from the reactant complexes. There is excellent agreement between the primary and secondary BDEs along with good agreement with theoretical hydration enthalpies for all levels examined here. Our best experimental results are believed to correspond to the measurement of primary dissociation thresholds as they have fewer uncertainties regarding the distribution of energy available to the dissociating species.

There are four distinct trends in the experimental and theoretical BDEs for the $Co^{2+}(H_2O)_x$ systems. The BDEs decrease rapidly from x = 4 to 5 as all waters are directly bound to the metal center in x = 4, whereas a second solvent shell is formed with a double accepting (AA) water in x = 5. The slight increase in BDEs from x = 5 to 6 indicates a change of coordination number (from

4 to 6) as all waters become bound directly to the metal center again at x = 6. Another large decrease indicating second solvent shell formation is observed from x = 6 to 7. For larger complexes, x = 7 - 11, the waters lost are all double acceptors in the second shell, such that their BDEs decrease slowly. MP2 theory is believed to account for the trends in these BDEs more accurately than DFT levels.

Charge separation (CS) processes are also observed as higher energy product pathways compared to water loss and become competitive primary dissociative pathways for x = 4, 6, and 7. The molecular parameters for the tight TSs associated with charge separation are calculated and used to analyze the product cross sections for the CID of $Co^{2+}(H_2O)_6$ and $Co^{2+}(H_2O)_7$ by including the competition between water loss and charge separation reactions to obtain accurate bond energies and CS barriers. Oddly, the charge separation of $Co^{2+}(H_2O)_6$ in reaction 9 is not observed in our CID of x = 5, an observation for which there is no ready explanation although several possibilities are forwarded. Experimental thresholds, in agreement with theory, determine that the $Co^{2+}(H_2O)_x$ critical size (according to the energetic definition) for competition between the CS and water loss pathways is $x_{crit} = 6$.

ACKNOWLEDGEMENT

Financial support was provided by the National Science Foundation, Grants No. Grants CHE-1664618. In addition, we thank the Center for High Performance Computing at the University of Utah for the generous allocation of computer time.

REFERENCES

- 1. T. E. Hofstetter and P. B. Armentrout, *J. Phys. Chem. A*, 2013, **117**, 1110-1123.
- 2. R. A. Coates and P. B. Armentrout, *J. Phys. Chem. A*, 2017, **121**, 3629-3646.
- 3. P. B. Armentrout and A. F. Sweeney, Eur. J. Mass Spectrom. (Chichester, Eng.), 2015, 21, 497-516.
- 4. T. E. Cooper, D. R. Carl and P. B. Armentrout, *J. Phys. Chem. A*, 2009, **113**, 13727–13741.
- 5. T. E. Cooper and P. B. Armentrout, *J. Phys. Chem. A*, 2009, **113**, 13742–13751.
- 6. T. E. Cooper and P. B. Armentrout, *Chem. Phys. Lett.*, 2010, **486**, 1-6.
- 7. T. E. Cooper and P. B. Armentrout, *J. Chem. Phys.*, 2011, **134**, 114308.
- 8. R. A. Coates and P. B. Armentrout, *J. Chem. Phys.*, 2017, **147**, 064305.
- 9. A. F. Sweeney and P. B. Armentrout, *J. Phys. Chem. A*, 2014, **118**, 10210-10222.
- 10. S. E. Rodriguez-Cruz, R. A. Jockusch and E. R. Williams, *J. Am. Chem. Soc.*, 1998, **120**, 5842-5843.
- 11. J. T. O'Brien and E. R. Williams, J. Phys. Chem. A, 2011, **115**, 14612-14619.
- 12. P. Jayaweera, A. T. Blades, M. G. Ikonomou and P. Kebarle, *J. Am. Chem. Soc.*, 1990, **112**, 2452-2454.
- 13. Z. L. Cheng, K. W. M. Siu, R. Guevremont and S. S. Berman, *J. Am. Soc. Mass Spectrom.*, 1992, **3**, 281-288.
- 14. A. A. Shvartsburg and K. W. M. Siu, *J. Am. Chem. Soc.*, 2001, **123**, 10071-10075.
- 15. M. Peschke, A. T. Blades and P. Kebarle, *J. Am. Chem. Soc.*, 2000, **122**, 10440-10449.
- 16. A. T. Blades, P. Jayaweera, M. G. Ikonomou and P. Kebarle, *Int. J. Mass Spectrom. Ion Processes*, 1990, **102**, 251-267.
- 17. A. T. Blades, P. Jayaweera, M. G. Ikonomou and P. Kebarle, *J. Chem. Phys.*, 1990, **92**, 5900-5906.
- 18. D. G. Barceloux, *J. Toxicol. Clin. Toxicol.*, 1999, **37**, 201-206.
- 19. L. Prashanth, K. K. Kattapagari, R. T. Chitturi, V. R. R. Baddam and L. K. Prasad, *J. Dr. NTR Univ. Health Sci.*, 2015, **4**, 75-85.
- 20. K. M. Ervin and P. B. Armentrout, *J. Chem. Phys.*, 1985, **83**, 166-189.
- 21. F. Muntean and P. B. Armentrout, *J. Chem. Phys.*, 2001, **115**, 1213-1228.
- 22. R. M. Moision and P. B. Armentrout, *J. Am. Soc. Mass Spectrom.*, 2007, **18**, 1124-1134.
- 23. S. A. Shaffer, D. C. Prior, G. A. Anderson, H. R. Udseth and R. D. Smith, *Anal. Chem.*, 1998, **70**, 4111-4119.
- 24. D. R. Carl, R. M. Moision and P. B. Armentrout, *J. Am. Soc. Mass Spectrom.*, 2009, **20**, 2312-2317.
- 25. C. E. Moore, *Atomic Energy Levels, NSRDS-NBS 35*, Washington, D. C., 1971.
- 26. D. R. Carl, B. K. Chatterjee and P. B. Armentrout, J. Chem. Phys., 2010, **132**, 1-12.
- 27. S. J. Ye and P. B. Armentrout, *J. Phys. Chem. A*, 2008, **112**, 3587-3596.
- 28. J. E. Carpenter, C. P. McNary, A. Furin, A. F. Sweeney and P. B. Armentrout, *J. Am. Soc. Mass Spectrom.*, 2017, DOI: 10.1007/s13361-017-1693-0.
- 29. T. E. Cooper, J. T. O'Brien, E. R. Williams and P. B. Armentrout, *J. Phys. Chem. A*, 2010, **114**, 12646–12655.
- 30. O. W. Wheeler, D. R. Carl, T. E. Hofstetter and P. B. Armentrout, *J. Phys. Chem. A*, 2015, **119**, 3800-3815.
- 31. D. Gerlich, Adv. Chem. Phys., 1992, **82**, 1-176.

- 32. N. Aristov and P. B. Armentrout, *J. Phys. Chem.*, 1986, **90**, 5135-5140.
- 33. N. F. Dalleska, K. Honma, L. S. Sunderlin and P. B. Armentrout, *J. Am. Chem. Soc.*, 1994, **116**, 3519-3528.
- 34. D. A. Hales and P. B. Armentrout, *J. Cluster Science*, 1990, **1**, 127-142.
- 35. N. R. Daly, Rev Sci Instrum, 1960, **31**, 264-267.
- 36. D. A. Hales, L. Lian and P. B. Armentrout, *Int. J. Mass Spectrom. Ion Processes*, 1990, **102**, 269-301.
- 37. R. H. Schultz, K. C. Crellin and P. B. Armentrout, *J. Am. Chem. Soc.*, 1991, **113**, 8590-8601.
- 38. T. S. Beyer and D. F. Swinehart, *Commun. ACM*, 1973, **16**, 379.
- 39. S. E. Stein and B. S. Rabinovich, *Chem. Phys. Lett.*, 1977, **49**, 183-188.
- 40. S. E. Stein and B. S. Rabinovitch, *J. Chem. Phys.*, 1973, **58**, 2438-2445.
- 41. R. G. Gilbert and S. C. Smith, *Theory of Unimolecular and Recombination Reactions*, Blackwell Scientific, London, 1990.
- 42. K. A. Holbrook, M. J. Pilling and S. H. Robertson, *Unimolecular Reactions*, Wiley, New York, 2nd edn., 1996.
- 43. D. G. Truhlar, B. C. Garrett and S. J. Klippenstein, *J. Phys. Chem.*, 1996, **100**, 12771-12800.
- 44. M. T. Rodgers, K. M. Ervin and P. B. Armentrout, *J. Chem. Phys.*, 1997, **106**, 4499-4508.
- 45. M. T. Rodgers and P. B. Armentrout, *J. Chem. Phys.*, 1998, **109**, 1787-1800.
- 46. P. B. Armentrout, *J. Chem. Phys.*, 2007, **126**, 234302.
- 47. P. B. Armentrout and J. Simons, *J. Am. Chem. Soc.*, 1992, **114**, 8627-8633.
- 48. N. F. Dalleska, K. Honma and P. B. Armentrout, *J. Am. Chem. Soc.*, 1993, **115**, 12125-12131.
- 49. R. M. Moision and P. B. Armentrout, *J. Phys. Chem. A*, 2002, **106**, 10350-10362.
- 50. A. D. Becke, J. Chem. Phys., 1993, **98**, 5648-5652.
- 51. R. Ditchfield, W. J. Hehre and J. A. Pople, *J. Chem. Phys.*, 1971, **54**, 724-728.
- 52. S. Grimme, S. Ehrlich and L. Goerigk, *J. Comput. Chem.*, 2011, **32**, 1456-1465.
- 53. J. P. Perdew, *Phys. Rev. B*, 1986, **33**, 8822-8824.
- 54. C. Möller and M. S. Plesset, *Phys. Rev.*, 1934, **46**, 618-622.
- 55. C. W. Bauschlicher and H. Partridge, *J. Chem. Phys.*, 1995, **103**, 1788-1791.
- 56. S. F. Boys and R. Bernardi, *Mol. Phys.*, 1970, **19**, 553-566.
- 57. F. B. van Duijneveldt, J. G. C. M. van Duijneveldt-van de Rijdt and J. H. van Lenthe, *Chem. Rev.*, 1994, **94**, 1873-1885.
- 58. K. P. Faherty, C. J. Thompson, F. Aguirre, J. Michne and R. B. Metz, *JPCA*, 2001, **105**, 10054-10059.
- 59. B. M. Marsh, J. M. Voss, J. Zhou and E. Garand, *Phys. Chem. Chem. Phys.*, 2015, **17**, 23195-23206.
- 60. R. Åkesson, L. G. M. Pettersson, M. Sandstrom, P. E. M. Siegbahn and U. Wahlgren, *J. Phys. Chem.*, 1992, **96**, 10773-10779.
- 61. H. S. R. Gilson and M. Krauss, *J. Phys. Chem. A*, 1998, **102**, 6525-6532.
- 62. R. D. Shannon, Acta Cryst., 1976, 32, 751-767.
- 63. M. K. Beyer and R. B. Metz, *J. Phys. Chem. A*, 2003, **107**, 1760-1762.

Table 1. Theoretical Relative Enthalpy (ΔH_0) and Free Energies $(\Delta G_{298})^a$ (kJ/mol) for Hydrated Cobalt Complexes a

	complex $(x,y,z)^b$	B3LYP	B3LYP-GD3BJ ^c	B3P86	MP2(full)
Co ²⁺ (H ₂ O) ₄	(4,0)	0.0 (0.0)	0.0 (0.0)	0.0 (0.0)	0.0 (0.0)
	$(3,1)_A$	52.8 (52.7)	56.6 (56.5)	50.8 (50.6)	80.5 (80.4)
$Co^{2+}(H_2O)_5$	(4,1)_AA	0.0(0.0)	0.0 (0.0)	0.0(0.0)	0.0(0.0)
	(5,0)	17.0 (26.4)	13.5 (22.8)	16.4 (25.8)	7.8 (17.1)
$Co^{2+}(H_2O)_6$	$(4,2)_4D_2AA$	0.0 (0.0)	3.0 (0.0)	0.0(0.0)	19.5 (12.7)
	$(5,1)_A_aA_b$	7.1 (10.1)	6.9 (6.8)	7.5 (10.5)	39.2 (35.4)
	$(6,0) D_{2h}$	4.9 (11.7)	0.0 (3.7)	5.8 (12.5)	0.0(0.0)
$Co^{2+}(H_2O)_7$	(4,3)_3D,DD_2AA,A	0.0(0.0)	4.5 (0.0)	0.0(0.0)	20.3 (17.4)
	(5,2)_2D,DD_2AA	9.2 (8.4)	7.2 (4.6)	8.0 (7.2)	11.6 (9.0)
	(6,1)_AA	6.8 (9.7)	0.0 (1.1)	7.0 (9.9)	0.0(0.0)
$Co^{2+}(H_2O)_8$	(4,4)_2D,2DD_2A,2AA	5.7 (8.6)	15.0 (18.0)	6.6 (9.6)	20.8 (20.6)
	$(5,3)_2D,2DD_3A_bA_b$	0.0(0.0)	4.3 (0.0)	0.0(0.0)	16.1 (12.9)
	$(6,2)_4D_2AA_t$	13.8 (17.0)	0.0 (2.0)	13.9 (17.0)	0.0(0.0)
$Co^{2+}(H_2O)_9$	(4,5)_D,3DD_2AA,3A	2.4 (8.9)	18.7 (21.9)	4.5 (10.9)	34.0 (37.2)
	(5,4)_2D,3DD_4AA	0.0(0.0)	4.5 (1.3)	0.0(0.0)	16.7 (13.4)
	$(6,3)_{6}D_{3}AA$	0.6 (3.9)	0.0 (0.0)	1.7 (5.0)	0.0(0.0)
$Co^{2+}(H_2O)_{10}$	(4,6)_4DD,2AA_4A	0.2 (6.7)	18.8 (23.8)	3.1 (9.6)	31.3 (36.4)
	(5,5)_D,4DD_4AA,A	0.0(0.0)	5.9 (4.5)	0.0(0.0)	15.8 (14.4)
	(6,4)_4D,2DD_4AA S ₄	3.2 (4.6)	0.0(0.0)	4.6 (6.0)	0.0(0.0)
$Co^{2+}(H_2O)_{11}$	(4,6,1)_4DD,4A_AA,AAD_A	6.1 (9.8)	28.4 (34.9)	5.4 (11.5)	42.6 (49.1)
	(5,5,1)_D,4DD_A,3AA,AAD_A	3.8 (1.3)	13.4 (13.8)	0.0 (0.0)	24.6 (25.0)
	(5,6)_5DD_4AA,2A	0.0 (0.0)	9.3 (12.2)	0.6 (3.1)	34.4 (37.3)
	(6,5)_2D,4DD_5AA	3.5 (0.5)	0.0 (0.0)	1.3 (0.9)	0.0(0.0)

 $[^]a\Delta G_{298}$ values are given in parentheses. Values are single-point energies calculated at the level shown using a 6-311+G(2d,2p) basis set from geometries optimized at the B3LYP/6-311+G(d,p) level except as noted. Zero point energy corrections are included. b To differentiate otherwise similar structures, several additions to the nomenclature were made: 1) the point group symmetry may be added; 2) subscripts "a" and "b" refer to apex and base sites in an inner shell of five waters; 3) O – M^{2+} – O angles denoted as subscript "g" (gauche) for angles between 45° and 135°, and "t" (trans) for angles >135°. c Geometries optimized at B3LYP-GD3BJ/6-311+G(d,p) level.

Table 2. Optimized Parameters from Analysis of Cross Sections for Collision-Induced Dissociation of $Co^{2+}(H_2O)_x^a$

$\frac{z}{x}$	Reactant	Product	$\sigma_0{}^b$	n^b	E_0^b (eV)	E_0^c (eV)	$\Delta S^{\dagger}_{1000}$
Λ	Reactant			71	(PSL)	(No RRKM)	$(^{\mathrm{J}}/_{\mathrm{mol}\ \mathrm{K}})$
5	(4,1)	$(4,0)^d$	7 (2)	0.8(0.1)	1.02 (0.07)	1.12 (0.09)	50 (21)
		$(3,0)^e$	10 (3)		2.76 (0.10)		38 (14)
6	(4,2)	$(4,1)^d$	58 (3)	0.8(0.1)	1.10 (0.08)	1.21 (0.10)	75 (31)
	(6,0)	$(4,1)^d$	59 (4)	0.8(0.1)	1.11 (0.07)	1.26 (0.11)	52 (32)
		$TS[3+2]^f$	4 (3)		0.97 (0.06)	1.56 (0.08)	58 (10)
		$(4,0)^g$	65 (4)		2.22 (0.09)		58 (5)
7	(4,3)	$(4,1)^d$	79 (7)	1.0(0.1)	0.77(0.07)	0.95 (0.09)	13 (18)
	(6,1)	$(6,0)^d$	73 (5)	1.0 (0.2)	0.80(0.08)	0.99 (0.11)	62 (22)
		$TS[3+3]^f$	1(1)		0.82 (0.10)	1.43 (0.15)	43 (15)
		$(4,1)^g$	74 (10)		1.93 (0.09)		24 (4)
8	(5,3)	$(4,3)^d$	62 (7)	1.0(0.1)	0.68 (0.07)	0.90 (0.10)	55 (14)
	(6,2)	$(6,1)^d$	62 (7)	1.0 (0.1)	0.70 (0.06)	0.94 (0.10)	61 (43)
		$(6,0)^e$	60 (4)		1.56 (0.08)		50 (5)
9	(5,4)	$(5,3)^d$	88 (3)	1.0(0.1)	0.58 (0.08)	0.92 (0.10)	55 (5)
	(6,3)	$(6,2)^d$	88 (3)	1.0 (0.2)	0.60(0.07)	0.82 (0.10)	67 (5)
		$(6,1)^e$	84 (8)		1.36 (0.09)		51 (12)
10	(5,5)	$(5,4)^d$	99 (7)	0.9(0.1)	0.45 (0.08)	1.00 (0.14)	7 (10)
	(6,4)	$(6,3)^d$	100 (6)	0.9(0.1)	0.48 (0.07)	0.98 (0.15)	30 (15)
		$(6,2)^e$	102 (9)		1.08 (0.09)		65 (14)
11	(5,5,1)	$(5,5)^d$	74 (9)	1.2 (0.3)	0.40(0.08)	0.99 (0.14)	32 (10)
	(5,6)	$(5,5)^d$	75 (8)	1.2 (0.3)	0.40 (0.08)	0.98 (0.15)	2 (8)
	(6,5)	$(6,4)^d$	75 (9)	1.2 (0.3)	0.42 (0.07)	1.01 (0.15)	64 (22)
		$(6,3)^e$	77 (16)		1.05 (0.10)		34 (14)

^aUncertainties in parentheses. ^bParameters for modeling with lifetime effects (PSL) considered. ^cParameters for modeling where lifetime effects are not included. ^dSingle channel modeling of total cross section using eq 4. ^eSequential modeling of primary and secondary cross sections using eqs 4 × 6. ^fCompetitive analysis modeling of primary water loss and charge separation cross sections using eq 4. ^gCompetitive sequential analysis modeling of primary water and charge separation losses and secondary water loss cross sections using eqs 4 and 4 × 6.

Table 3. Comparison of Experimental and Theoretical 0 K Hydration Enthalpies (kJ/mol) for Co²⁺(H₂O)_x

x	Reactant	Product	Primary ^a	Secondary ^a	$B3LYP^b$	B3LYP-GD3BJ ^c	B3P86 ^b	MP2(full) ^b
1	(1,0)	Co^{2+}			408.4 (442.8)	415.2 (418.4)	410.0 (443.0)	498.8 (402.3)
2	(2,0)	(1,0)			326.6 (329.9)	331.7 (335.0)	330.2 (333.6)	310.1 (320.4)
3	(3,0)	(2,0)			228.8 (232.0)	234.9 (238.0)	233.3 (236.5)	211.6 (221.5)
4	(4,0)	(3,0)		167.6 ± 7.7	174.4 (177.4)	183.0 (186.0)	178.0 (181.1)	190.9 (200.6)
5	(4,1)	(4,0)	100.0 ± 6.4	109.5 ± 8.0	101.0 (104.2)	109.1 (112.2)	105.1 (108.3)	98.8 (108.1)
6	(6,0)	(4,1)	107.3 ± 7.3	108.7 ± 6.0	91.4 (94.8)	107.0 (110.3)	94.0 (97.4)	111.4 (124.1)
7	(6,1)	(6,0)	77.3 ± 7.5	84.1 ± 6.4	77.4 (80.1)	85.1 (87.8)	80.7 (83.5)	76.1 (84.3)
8	(6,2)	(6,1)	67.7 ± 5.8	$74.1\ \pm7.5$	72.7 (75.5)	80.1 (82.8)	65.6 (78.8)	82.1 (92.0)
9	(6,3)	(6,2)	57.7 ± 6.6	64.3 ± 8.8	76.3 (79.2)	83.0 (85.9)	78.2 (81.1)	77.4 (85.7)
10	(6,4)	(6,3)	45.9 ± 7.0	60.0 ± 8.7	59.2 (61.9)	67.2 (69.9)	61.5 (64.2)	60.0 (66.9)
11	(6,5)	(6,4)	40.2 ± 7.1		56.4 (58.9)	65.9 (68.4)	58.9 (61.4)	59.5 (66.4)
MAD^d			6.8^{e}	7.9	9.5 (11.4)	14.1 (17.3)	11.2 (14.0)	8.8 (17.0)
MAD^f				7.6^{e}	7.1 (6.8)	6.8 (9.5)	8.1 (7.5)	8.8 (12.0)

^aValues from Table 2. ^bTheoretical values with (and without) cp correction. Single point energies calculated at the indicated level of theory using 6-311+G(2d,2p) basis set using B3LYP/6-311+G(d,p) geometries and zero point energy corrected. ^cSingle point energies calculated at the indicated level of theory using 6-311+G(2d,2p) basis set using B3LYP-GD3BJ/6-311+G(d,p) geometries and zero point energy corrected. ^dMean absolute deviations from primary experimental BDEs. ^eMean experimental uncertainty. ^fMean absolute deviations from secondary experimental BDEs.

Table 4. Conversion of 0 K Thresholds to 298 K Enthalpies and Free Energies (kJ/mol) for Co²⁺(H₂O)_x^a

x	Reactant	Product	$\Delta { m H}_0{}^b$	ΔH_{298} - ΔH_0^c	ΔH_{298}	$T\DeltaS_{298}{}^{c}$	ΔG_{298}
4	(4,0)	(3,0)	167.6 (7.7)	-3.7 (0.9)	163.9 (7.7)	24.6 (2.3)	139.3 (8.6)
5	(4,1)	(4,0)	98.9 (6.4)	4.5 (0.4)	103.4 (6.4)	39.3 (1.0)	64.1 (6.7)
6	(6,0)	(4,1)	107.3 (7.3)	-0.8 (0.7)	106.4 (7.3)	43.7 (1.1)	62.8 (8.6)
		TS[3+2]	93.9 (5.6)	3.5 (0.5)	97.4 (5.6)	20.8 (0.4)	76.6 (5.6)
7	(6,1)	(6,0)	77.3 (7.5)	3.6 (0.4)	80.9 (7.5)	36.8 (1.0)	44.1 (8.0)
		TS[3+3]	79.0 (9.3)	4.8 (0.5)	83.7 (9.4)	28.4 (0.3)	55.4 (9.7)
8	(6,2)	(6,1)	67.7 (5.8)	3.6 (0.4)	71.3 (5.8)	40.3 (1.0)	30.9 (6.2)
9	(6,3)	(6,2)	57.7 (8.3)	4.5 (0.5)	62.3 (8.3)	44.1 (1.0)	18.2 (9.0)
10	(6,4)	(6,3)	45.9 (7.9)	2.2 (0.4)	48.1 (7.9)	33.9 (1.2)	14.1 (8.5)
11	(6,5)	(6,4)	40.2 (10.8)	3.4 (0.4)	43.6 (10.8)	43.5 (1.1)	0.04 (10.9)

^aUncertainties in parentheses. ^bValues from Table 2. ^cValues are calculated from the vibrational frequencies and rotational constants calculated at the B3LYP/6-311+G(d,p) level of theory. Uncertainties are found by scaling the vibrational frequencies up and down by 10%.

Table 5. Comparison of 0 K Transition State Energies and Hydration Enthalpies (kJ/mol)

x	Reactant	Product	Experiment	B3LYP ^a	B3LYP- GD3BJ ^b	B3P86 ^a	MP2(full) ^a
4	(4,0)	(3,0)	168 ± 8^c	177.4	186.0	181.1	200.6
		TS[2+1]		126.0	134.6	127.2	156.9
		$CoOH^+(H_2O)_2 + H^+H_2O$		-37.3	-27.8	-35.8	7.7
5	(4,1)	(4,0)	100 ± 6^c	104.2	112.2	108.3	108.1
		TS[(3,2)-(3,1,1)]		109.0	116.6	110.2	117.8
		TS[2+2]		77.2	89.3	77.5	117.3
		$CoOH^{+}(H_2O)_2 + H^{+}(H_2O)_2$		-79.6	-65.9	-79.7	-47.6
		TS[3+1]		123.6	132.1	125.6	142.3
		$CoOH^+(H_2O)_3 + H^+H_2O$		-30.2	-21.2	-29.8	-4.1
6	(6,0)	(4,1)	107 ± 7^c	94.8	110.3	97.4	124.1
		TS[3+2]	94 ± 6^d	66.5	86.2	65.9	117.0
		$CoOH^{+}(H_2O)_3 + H^{+}(H_2O)_2$		-81.9	-61.2	-84.7	-23.5
7	(6,1)	(6,0)	77 ± 8^c	80.1	87.8	83.5	65.6
		TS[3+3]	79 ± 9^d	59.8	83.3	60.5	93.5
		$CoOH^{+}(H_{2}O)_{3} + H^{+}(H_{2}O)_{3}$		-87.9	-63.1	-89.0	-45.9

^aSingle point energies corrected for zero point energy calculated at the indicated level of theory using 6-311+G(2d,2p) basis set with geometries and vibrational frequencies calculated at the B3LYP/6-311+G(d,p) level. ^bSingle point energies corrected for zero point energy calculated 6-311+G(2d,2p) basis set with geometries and vibrational frequencies calculated at the B3LYP-GD3BJ/6-311+G(d,p) level. ^cValues taken from Table 2, using the primary dissociation channel model for x = 5 - 7 and the sequential model for x = 4. ^dValues taken from Table 2 calculated by competitive analysis model (eq 4).

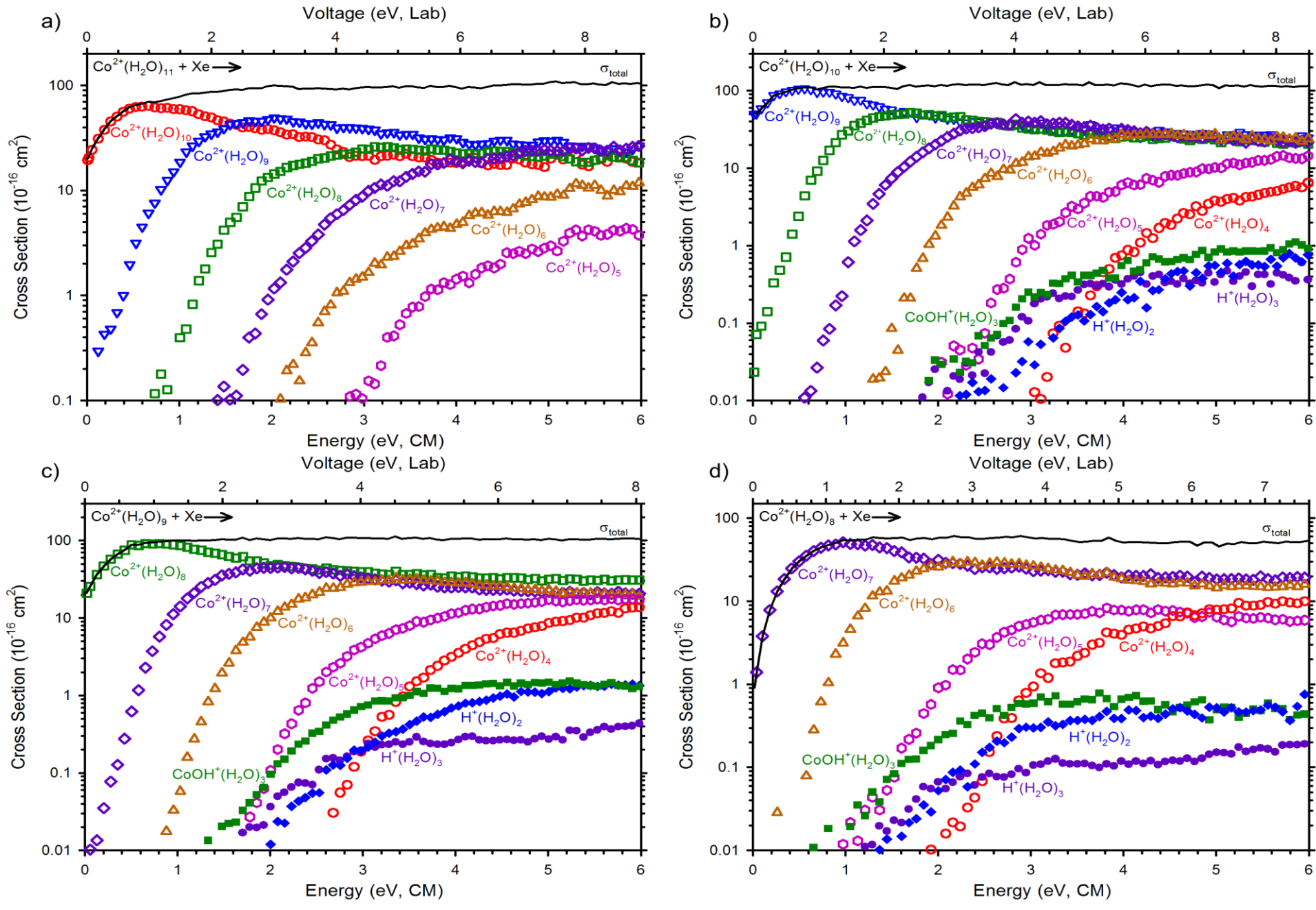


Figure 1.



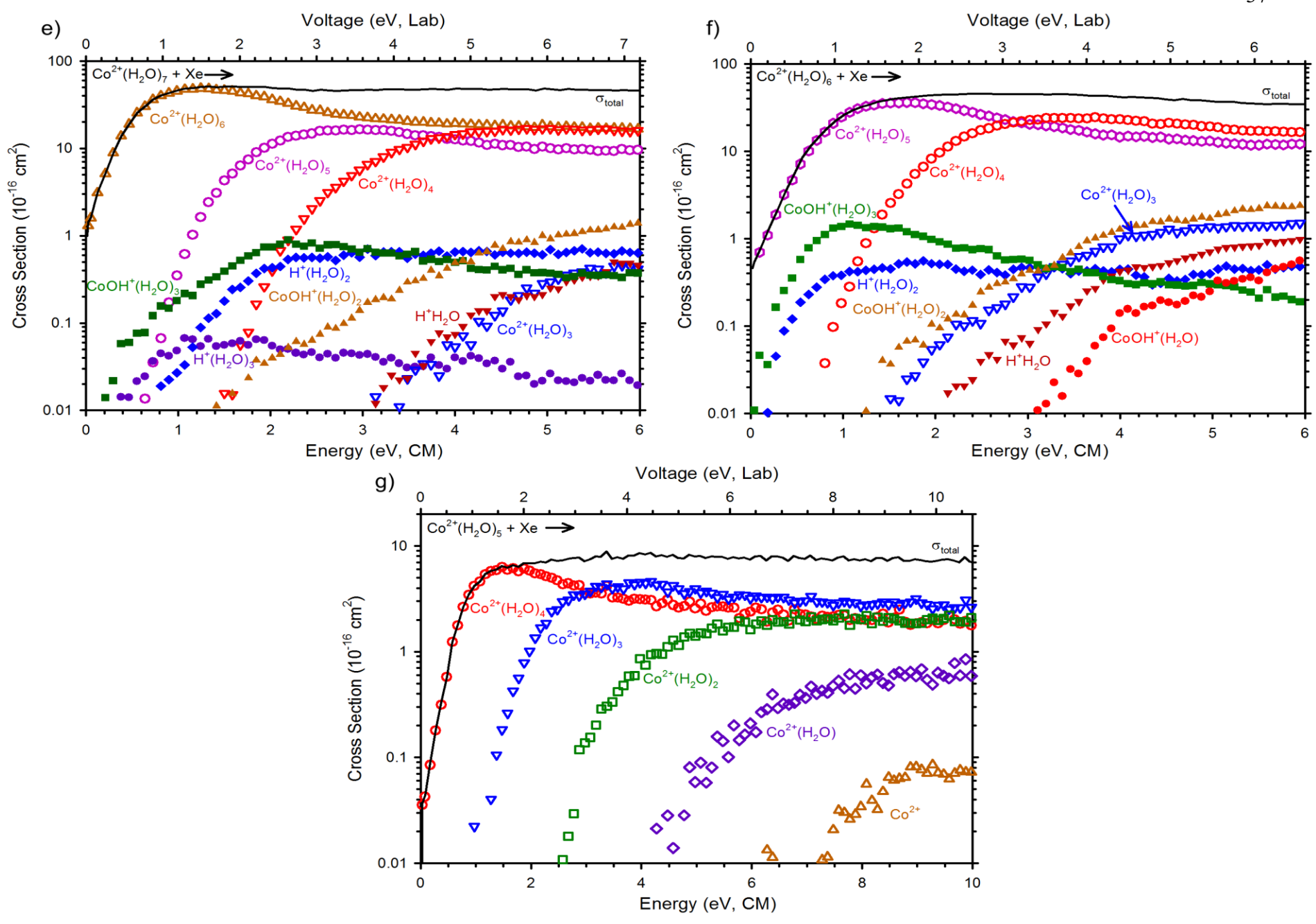


Figure 1. Cross sections for collision-induced dissociation of $Co^{2+}(H_2O)_x$ where x = 11 - 5 (parts a - g) with Xe (~ 0.2 mTorr) as a function of kinetic energy in the center-of-mass frame (bottom x-axis) and applied voltage in the laboratory frame (top x-axis). Water loss products are represented by open symbols and charge separation products by closed symbols.

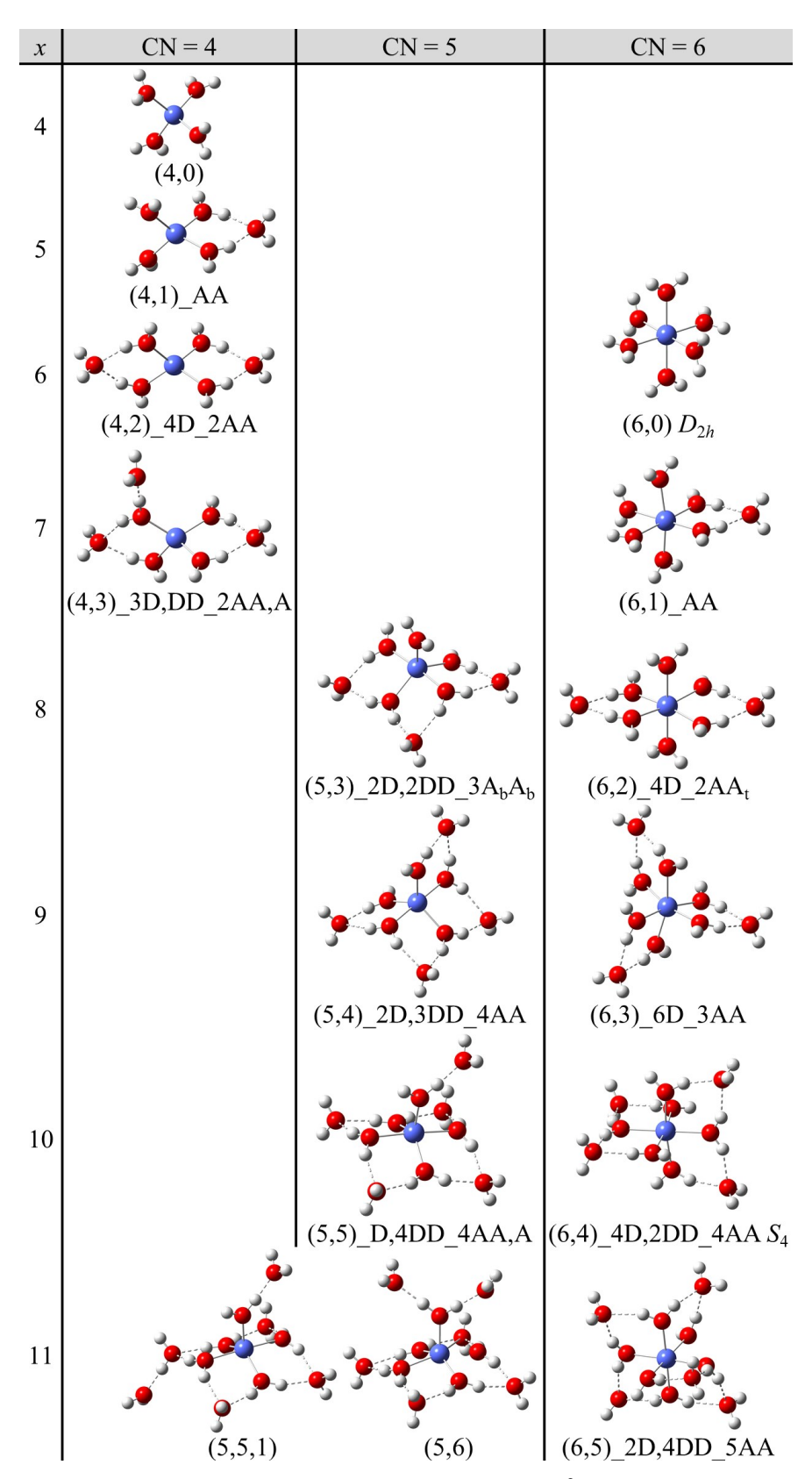


Figure 2. Geometries for the predicted ground structures of $Co^{2+}(H_2O)_x$ complexes, x = 4 - 11, as optimized at the B3LYP/6-311+G(d,p) level of theory.

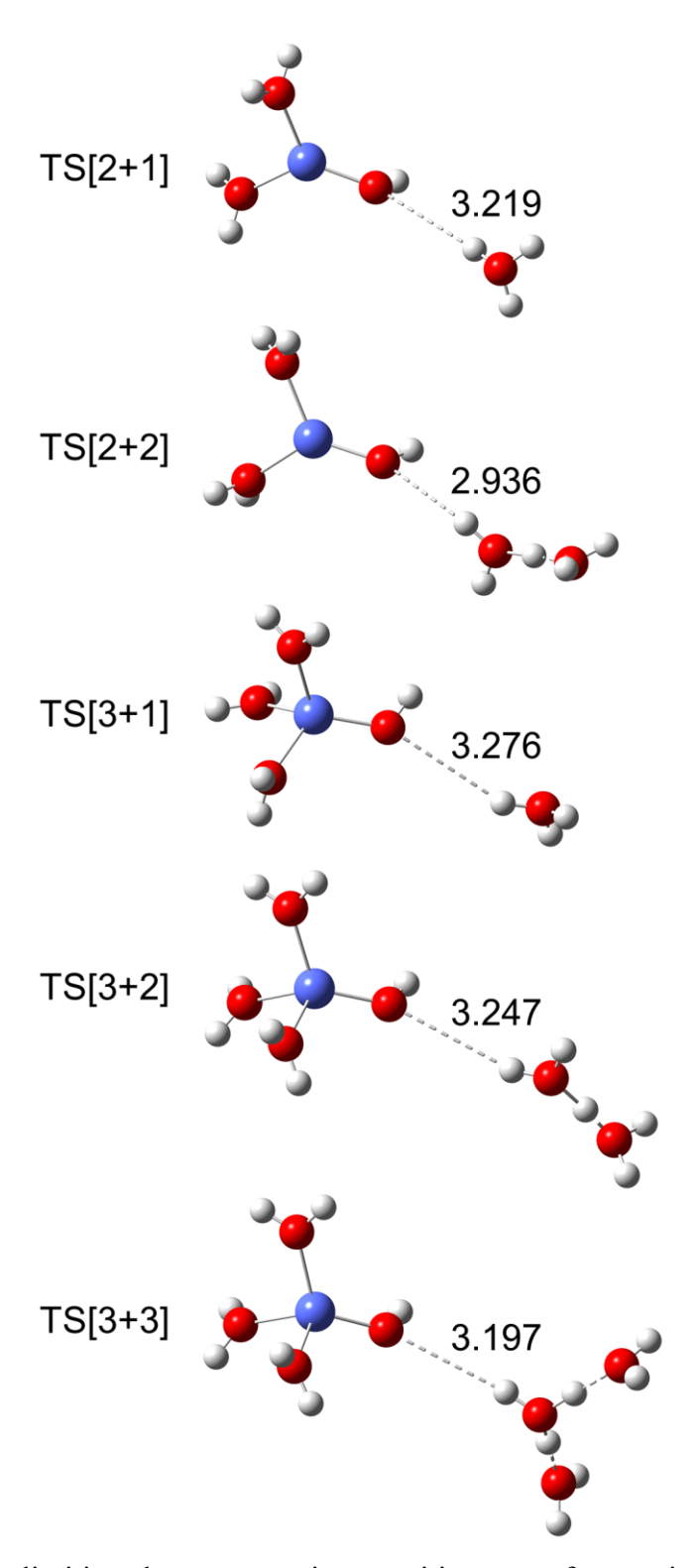


Figure 3. Possible rate-limiting charge separation transition states for reactions 7-9 and those for x = 5. Structures were optimized at the B3LYP/6-311+G(d,p) level of theory. Brackets denote TS[x+y] naming scheme where x indicates the number of waters directly bound to the CoOH⁺ center and y indicates the number of waters bound to the leaving H⁺. Bond lengths for the O-H⁺ bond being broken (dashed line) are provide in Angstroms (Å).

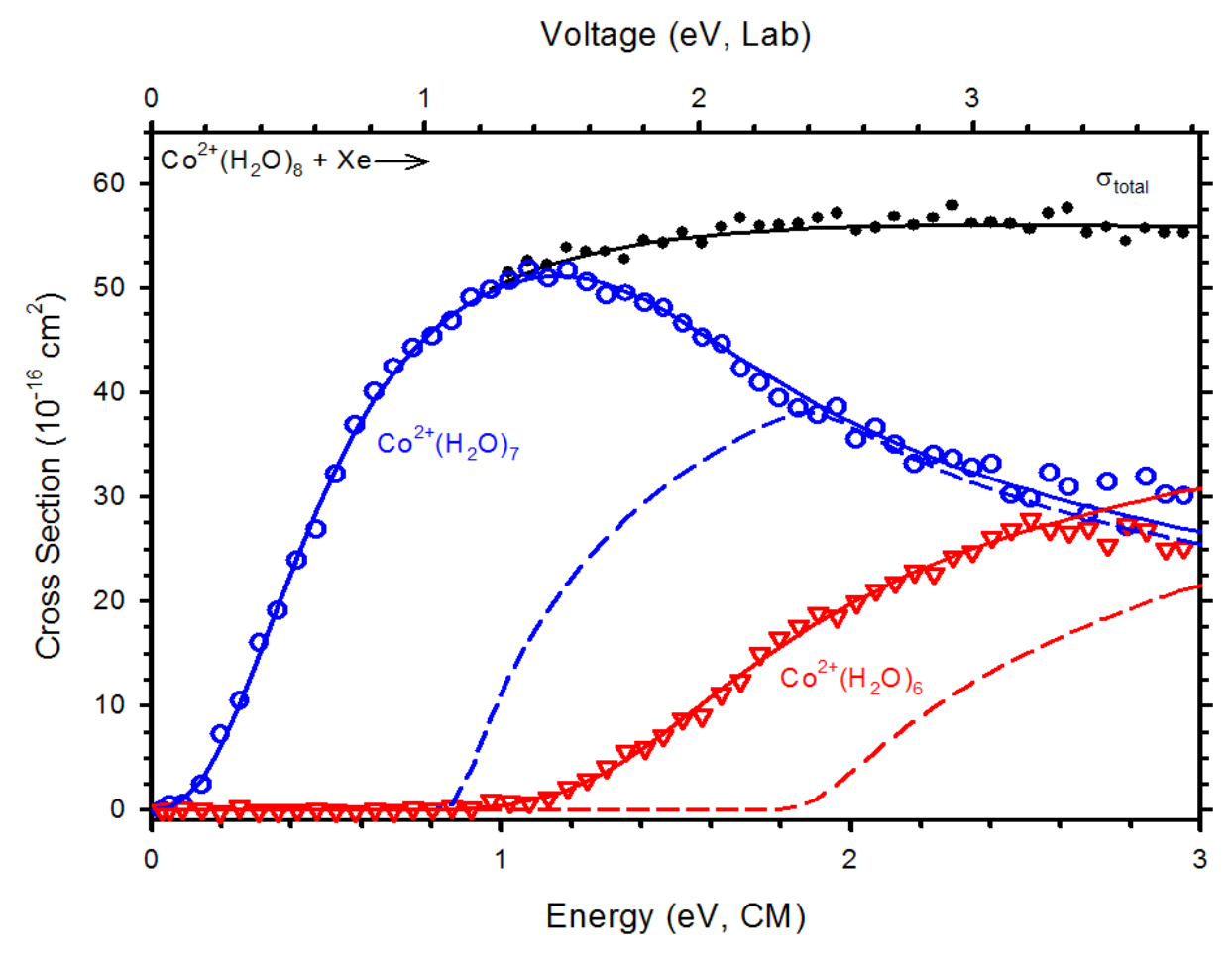


Figure 4. Zero-pressure extrapolated cross sections for the CID of $Co^{2+}(H_2O)_8$. Solid lines show the best fits to the primary (open circles) and secondary (open triangles) water loss cross sections using eq 4 × 6 for the sequential model convoluted over the neutral and ion kinetic and internal energy distributions. Dashed lines show the models in the absence of experimental kinetic energy broadening for reactants with an internal energy of 0 K. Optimized parameters for these fits are found in Table 2.

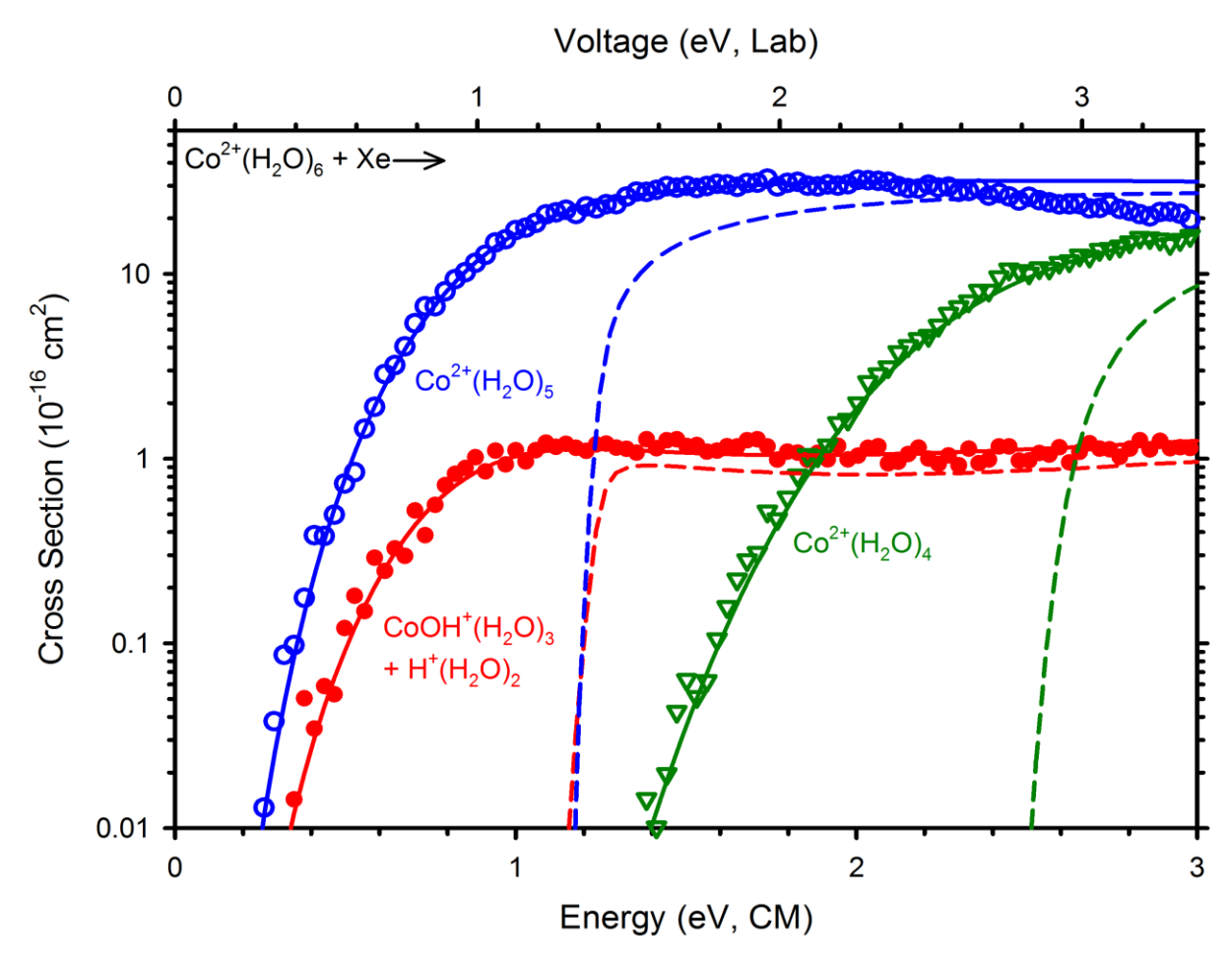


Figure 5. Zero-pressure extrapolated cross sections for the CID of $Co^{2+}(H_2O)_6$. Solid lines show the best fits to the primary water loss (open circles), the competing charge separation products (closed circles), and secondary water loss (open triangles) using eq 4 and eq 4 \times 6 for the competitive sequential model convoluted over the neutral and ion kinetic and internal energy distributions. The dashed lines show the models in the absence of experimental kinetic energy broadening for reactants with an internal energy of 0 K. Optimized parameters for these fits are found in Table 2.

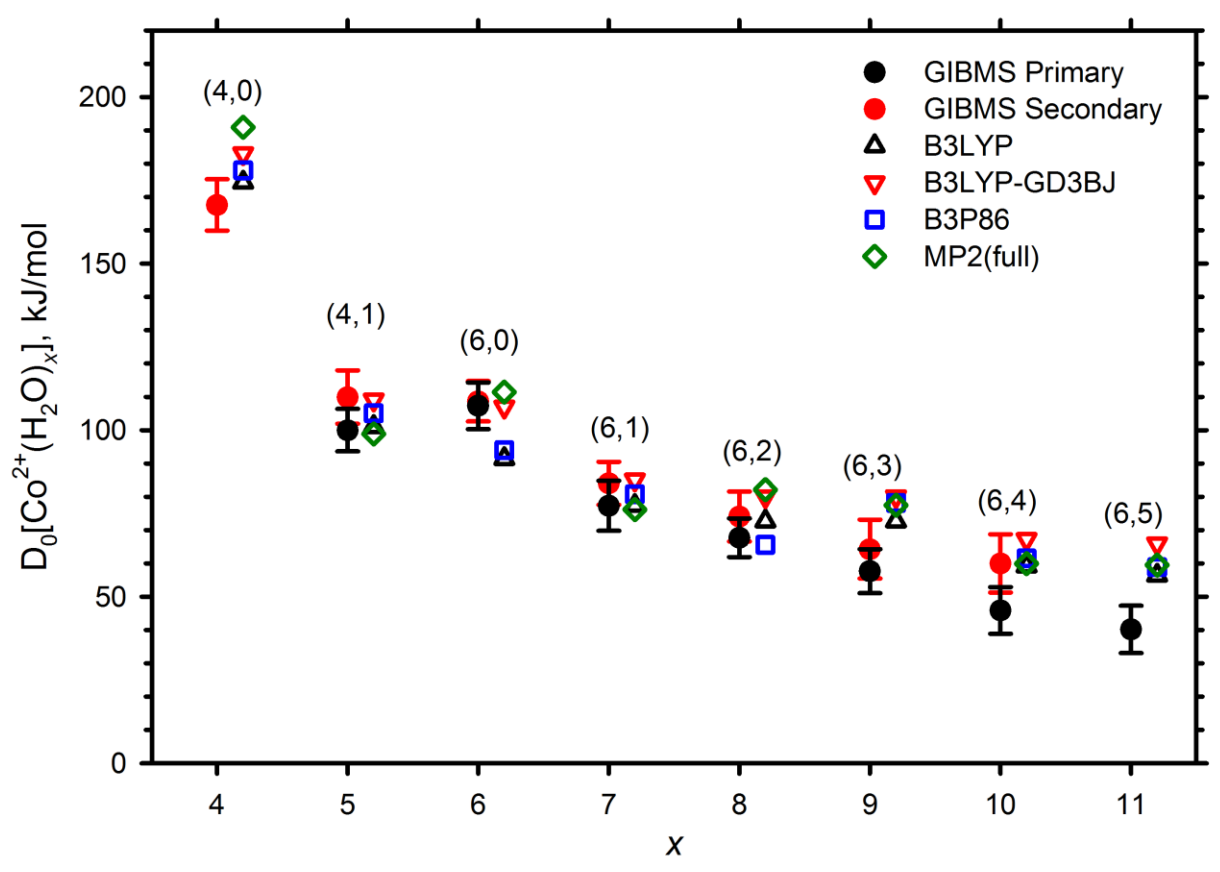


Figure 6. Comparison of experimental primary (black solid circles) and secondary (red solid circles) 0 K bond energies with theoretical B3LYP (open black up triangles), B3LYP-GD3BJ (open red down triangles), B3P86 (open blue squares) and MP2 values (open green diamonds), including cp corrections.

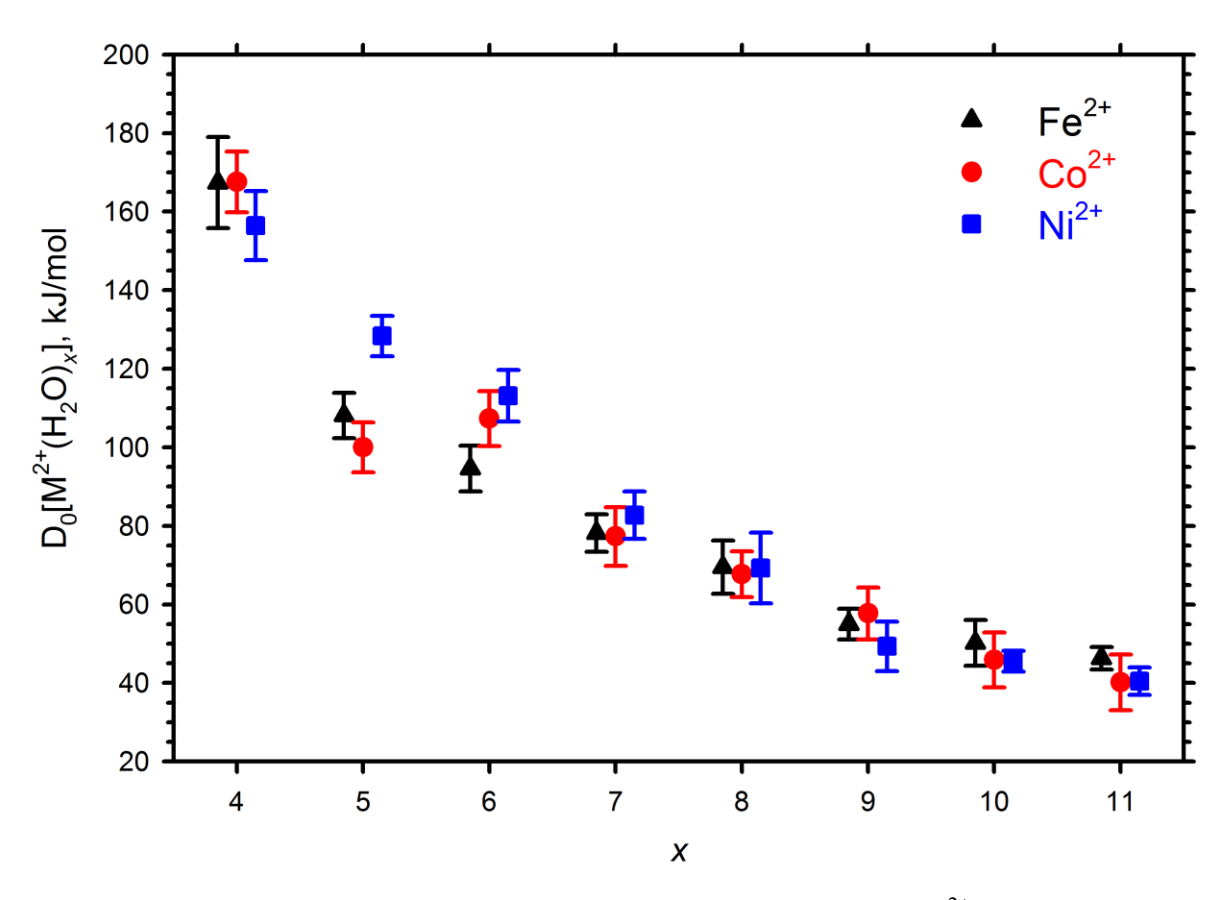


Figure 7. Comparison of experimental primary 0 K bond energies for $Fe^{2+}(H_2O)_x$ (black triangles, reference 1), $Co^{2+}(H_2O)_x$ (red circles, present work), and $Ni^{2+}(H_2O)_x$ (blue squares, reference 2). All x = 4 values are secondary 0 K BDE values.

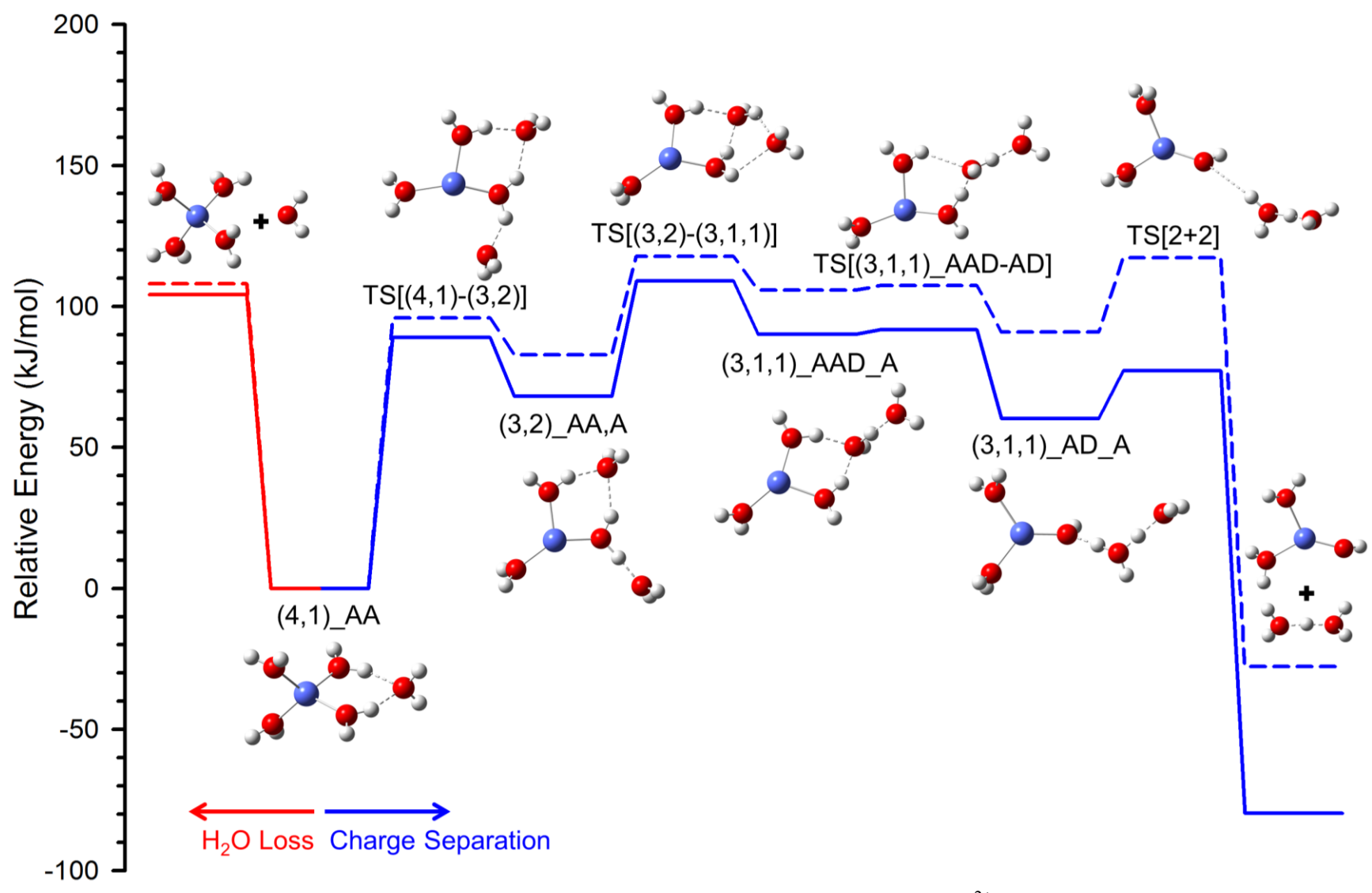


Figure 8. Reaction coordinates for water loss (red) and charge separation (blue) pathways of Co²⁺(H₂O)₅ from the (4,1)_AA GS. Single point energies are calculated at the B3LYP (solid line) and MP2 (dashed line) levels of theory with the 6-311+G(d,p) basis set and include zero point energies.